

UNIVERSITY OF LJUBLJANA
FACULTY OF MATHEMATICS AND PHYSICS
DEPARTMENT OF PHYSICS
MEDICAL PHYSICS

Aleksandar Bordelius

**TEST BEAM STUDIES OF SPACAL
PROTOTYPE CALORIMETER MODULE
WITH TUNGSTEN ABSORBER**

MASTER THESIS

ADVISER: doc. dr. Rok Dolenec
COADVISER: dr. Philipp Gerhard Roloff

Ljubljana, 2023

UNIVERZA V LJUBLJANI
FAKULTETA ZA MATEMATIKO IN FIZIKO
ODDELEK ZA FIZIKO
MEDICINSKA FIZIKA

Aleksandar Bordelius

**ŠTUDIJE "SPACAL" PROTOTIPNEGA
KALORIMETRSKEGA MODULA IZ
VOLFRAMOVEGA ABSORBERJA V
TESTNEM ŽARKU POSPEŠENIH DELCEV**

Magistrsko delo

MENTOR: doc. dr. Rok Dolenec
SOMENTOR: dr. Philipp Gerhard Roloff

Ljubljana, 2023

Acknowledgements

Research work generally requires a collective effort. Herein, I express my sincere gratitude to my dear colleagues, friends, and family members who have supported me in various ways during my thesis work.

First, I want to thank my supervisor, Rok Dolenc, and my co-supervisor, Philipp Gerhard Roloff, for their guidance throughout the research process. Their valuable comments, corrections, and improvements to my thesis, as well as many helpful discussions greatly contributed to its progress.

Next, I want to say thank you to Loris Martinazzoli, Matteo Salomoni, and Marco Pizzichemi. Loris supervised my work since the very beginning when I first came to CERN as a summer student. I learned a lot from him about test beam data analysis, calorimetry, and SpaCal technologies, and we concluded many studies on time resolution and energy resolution together. With Matteo, we spent many days in the lab setting up the linearity measurement bench and in the workshop assembling the new SpaCal prototype. He taught me a lot about photodetectors, PMTs in particular, and how to safely work with lasers and other equipment such as high-voltage power supplies, oscilloscopes, and optical equipment. Here I also want to thank our young technician, Kacper Jama, for his work on the new SpaCal prototype and the many mechanical designs needed in the linearity measurement bench. Thanks to Marco and his detailed instructions, I could use the simulation software without many difficulties and got simulation results of the new SpaCal prototype very quickly. It goes without saying that I appreciate the help and company of the many other people I did not name above, but I've met since I was warmly welcomed to CERN and became a member of the PicoCal group. Again, thank you all!

Before I end this paragraph, I must thank my family. Throughout my studies, our relationships had many ups and downs, we fought and reconciled, and it was all for me to learn that I definitely love them. Now that our family has grown by one member, and I got my duties as an uncle, supporting one another is as essential as ever. I hope we can laugh, have fun, experience new things together, and be close to one another for many days yet to come. Thank you so much!

Študije "SpaCal" prototipnega kalorimetskega modula iz volframovega absorberja v testnem žarku pospešenih delcev

IZVLEČEK

Elektromagnetni kalorimeter ECAL je pod-detektor univerzalnega detektorja za fiziko okusov LHCb, ki deluje na pospeševalniku LHC v Evropskem laboratoriju za fiziko delcev - CERN. Ena tretjina vseh razpadnih produktov delcev s težjimi kvarki je π_0 mezonov oziroma nevtralnih delcev, po razpadu katerih nastanejo gama fotoni. Ti fotoni imajo energije od nekaj GeV do več 100 GeV, zato je visoko-zmogljivi elektromagnetni kalorimeter ključnega pomena za LHCb eksperiment. Vzorčevalni tip kalorimetra je bil izbran kot najboljši kandidat in kompromis med energijsko ločljivostjo, zmožnostjo zaznavanja kompaktnih elektromagnetnih plazov, hitrim časovnim odzivom in sprejemljivo ceno.

Leta 2022 je bila predlagana pomembna nadgradnja LHCb ECAL sistema, tako imenovana nadgradnja II, ki vključuje tudi nadgradnjo ostalih pod-detektorjev LHCb eksperimenta. Po nadgradnji II bo LHCb detektor zajemal podatke pri veliko višji luminoznosti kot dosedaj do okoli $1.5 \times 10^{34} \text{ cm}^{-2} \text{ s}^{-1}$. To postavlja nove stroge zahteve za kalorimeter, predvsem potrebo po boljši granularnosti in časovnem odzivu velikostnega reda nekaj 10 ps.

Kot eden izmed kandidatov za nadgradnjo II LHCb ECAL se razvija novi tip SpaCal (angl. *Spaghetti Calorimeter*) kalorimetra. V tem magistrskem delu preučujem zmogljivost SpaCal prototipnega modula z volframovim absorberjem in plastičnimi scintilacijskimi vlakni na podlagi meritev, zajetih v testnem žarku pospešenih delcev, dostopnim v CERN-u in DESY-u, in dodatno validacijo s simulacijami. Prototip doseže energijsko ločljivost $\sim 9.75\%/\sqrt{E} \oplus 1.26\%$ in časovno ločljivost ~ 20 ps pri 100 GeV. Z dodatno študijo časovnega odziva pokažem, da je časovni odziv homogen po večjem območju celice kalorimetra.

Ključne besede: elektromagnetni kalorimeter, volframov absorber, pikosekundna časovna ločljivost, študije v testnem žarku pospešenih delcev

Test beam studies of SpaCal prototype calorimeter module with tungsten absorber

ABSTRACT

The electromagnetic calorimeter, ECAL, is a sub-detector of the general-purpose flavor physics experiment, LHCb, operating at the LHC accelerator at the European Organization for Nuclear Research - CERN. Since one-third of heavy flavor decay products are π_0 mesons or other neutral particles decaying to photons in a wide energy range from a few GeV to several 100 GeV, a high-performance electromagnetic calorimeter is essential in LHCb. A scintillating sampling calorimeter has been chosen as a good compromise between energy resolution, ability to detect compact electromagnetic showers, fast time response, and moderate price.

In 2022, a significant upgrade to the LHCb ECAL system has been proposed, so-called Upgrade II, which includes the upgrade of other sub-detectors of the LHCb experiment. At Upgrade II conditions, the LHCb detector will take data at a much higher luminosity as of now, of up to $1.5 \times 10^{34} \text{ cm}^{-2} \text{ s}^{-1}$. This puts new severe requirements on the calorimeter, in particular, the need for better granularity and time response of O(10) ps.

As one of the candidates for the Upgrade II of the LHCb ECAL, a new type of Spaghetti Calorimeter (SpaCal) is being developed. In this thesis, I study the performance of a module-size SpaCal prototype with a tungsten absorber and plastic scintillating fibers through test beams at CERN and DESY and through simulation validations. The prototype achieves an energy resolution of $\sim 9.75\%/\sqrt{E} \oplus 1.26\%$ and a time resolution of ~ 20 ps at 100 GeV. The time response is further studied, and I show it to be homogeneous over a large area within a calorimeter cell.

Keywords: electromagnetic calorimeter, tungsten absorber, picosecond time resolution, test beam studies

Contents

1	Introduction	13
1.1	The LHCb Experiment	13
1.1.1	The LHCb detector after Upgrade I	14
1.1.2	Upgrade II of the LHCb experiment	16
2	Calorimetry in particle physics	19
2.1	Passage of radiation through matter	20
2.1.1	Energy loss of electrons and positrons	20
2.1.2	Interactions of photons with matter	22
2.1.3	Physics of an electromagnetic cascade	23
2.2	Scintillation-based sampling calorimeters	24
2.2.1	Operation of scintillation detectors	25
2.3	Energy resolution of a calorimeter	26
2.4	Electromagnetic calorimeter of the LHCb	29
3	SpaCal with tungsten absorber	31
3.1	SpaCal technologies	32
3.2	Assembly of a new SpaCal WPoly prototype	33
3.2.1	Development and production of the support structure	34
3.2.2	Fiber cutting	34
3.2.3	Fiber insertion	35
3.2.4	Fiber gluing	36
3.2.5	Fiber polishing	36
3.2.6	Development and installation of calibration system	37
3.2.7	Development and production of hollow light guides	37
3.2.8	Development and production of PMT holders	38
3.2.9	Characterization of PMT voltage divider boards	38
3.2.10	PMT installation	39
3.3	Photodetector characterization	40
3.3.1	Response non-linearity measurements	40
4	Test beam results	45
4.1	Test beam setup	45
4.2	Time resolution	47
4.2.1	Scan for optimal voltage	48
4.2.2	Scan for optimal CFD threshold	49
4.2.3	Time resolution with respect to beam energy	51
4.2.4	Spatial homogeneity of time response	53
4.3	Energy resolution	55

4.3.1	Energy resolution with respect to inclination angle	55
4.3.2	Energy resolution at energies from 1 to 100 GeV	59
5	Simulation studies	61
5.1	Simulation framework	61
5.2	Energy resolution of the new SpaCal prototype	62
5.2.1	Comparison in the energy range from 1 to 100 GeV	63
6	Conclusion	65
7	Bibliography	67
	Razširjeni povzetek v slovenskem jeziku	71

1. Introduction

The Large Hadron Collider (LHC) is the world's largest and most powerful particle accelerator. It started operating on the 10th of September in 2008 and remains the latest addition to the CERN accelerator complex. The LHC consists of a 27-kilometer ring built with superconducting magnets and a number of accelerating structures to boost the energy of the particles along the way. Inside the accelerator, two high-energy particle beams circle around at close to the speed of light before they collide at four locations around the accelerator ring, corresponding to the positions of four particle detectors - ATLAS, CMS, ALICE, and LHCb [1].

The High-Luminosity Large Hadron Collider (HL-LHC) project aims to enhance the performance of the LHC in order to increase the potential for discoveries after 2028. The objective is to increase the integrated luminosity by a factor of 5-7 beyond the LHC design value. Luminosity is an important performance trait of an accelerator: it is proportional to the number of collisions that occur in a given amount of time. The higher the luminosity, the faster the experiments can gather to allow them to observe rare processes [2].

However, to benefit from the increase in luminosity, the detectors at the LHC have to prepare adequately for this enhancement. In practice, this means upgrading underlying sub-detectors of the experiment to meet the requirements the increase in luminosity imposes on the detector. For example, in the case of electromagnetic calorimeters, some of the requirements are better granularity in the central region, higher radiation tolerance, and improved timing capabilities.

1.1 The LHCb Experiment

The Large Hadron Collider beauty (LHCb) experiment is one of the four large detectors constructed around the LHC accelerator at CERN, and its primary purpose is to search for new physics through studies of CP-violation and rare decays of heavy-flavor hadrons. The detector is a forward-facing spectrometer detecting particles emitted in the pseudorapidity range $2 < \eta < 5$. The first sub-detector is mounted close to the collision point, with the others following over a length of 20 meters [3].

During the Long Shutdown 2 (LS2) lasting from 2018 to 2022, the LHCb experiment upgraded its detector with the so-called Upgrade I, discussed in chapter 1.1.1. At the beginning of 2026, the experiment plans another upgrade, LHCb Upgrade II, discussed in chapter 1.1.2. This upgrade will again allow the experiment to collect data at an even higher luminosity compared to the previous detector designs.

1.1.1 The LHCb detector after Upgrade I

The LHCb Upgrade I, carried out between 2018 and 2022, presents a major change in the experiment. It includes almost a complete renewal of the sub-detectors to allow running at an instantaneous luminosity five times larger than that of the previous running periods. The main highlights of the upgrade are the following [4]:

- A change in the readout of all sub-detectors into an all-software trigger is central to the new design, facilitating the reconstruction of events at the maximum LHC interaction rate and their selection in real-time. The first stage of the all-software trigger was implemented on a GPU farm.
- An upgrade of the experiments tracking system with the addition of a new pixel vertex detector, a silicon tracker upstream of the dipole magnet, and three scintillating fiber tracking stations downstream of the magnet.
- A new system of photodetectors was installed in the RICH detectors.
- Calorimeter and muon systems renewed their readout electronics.

The upgraded detector shown in figure 1.1 is designed to run at a nominal instantaneous luminosity $\mathcal{L} = 2 \times 10^{33} \text{ cm}^{-2} \text{ s}^{-1}$ and to collect events at the LHC crossing rate of 40 MHz. With the instantaneous luminosity increase by a factor of five and by improving the trigger efficiency for most of the modes by a factor of two, the annual yields in most channels are expected to be an order of magnitude larger than for the previous LHCb experiment. A total integrated luminosity (including Run 1 and 2) of around 60 fb^{-1} is expected by the end of Run 4 (in 2025) of the LHC [4].

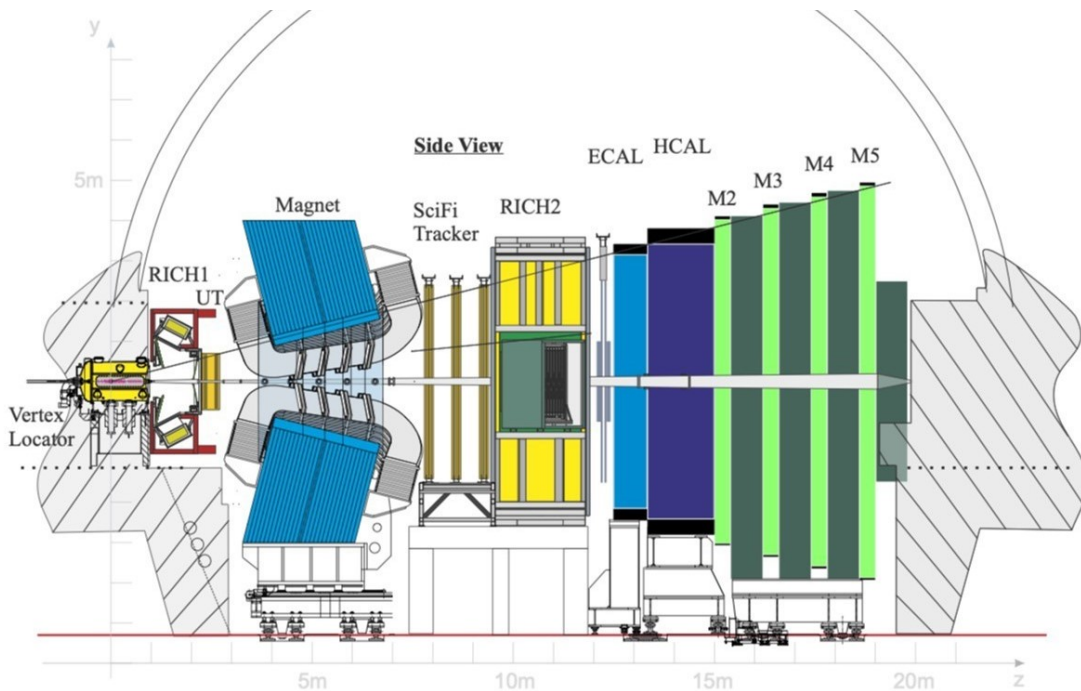


Figure 1.1: Schematic side-view of the Upgrade I LHCb detector [4].

The core technology of the new Vertex Locator (VELO) are pixelated hybrid silicon detectors, which are arranged into 52 modules and cooled by a silicon microchannel cooler. The VELO detects tracks of ionizing particles coming from the beam collision region to measure the location of interaction vertices, displaced decay vertices, and the distances between them. VELO tracks seed the reconstruction algorithm of the LHCb detector and provide discriminatory information for event selection [4].

In LHCb, the RICH system provides hadron particle identification (PID) in the 2.6-100 GeV/ c momentum range. It allows distinguishing between final states of otherwise identical topologies, heavily reducing the combinatorial background in decay modes involving hadrons in the final state. RICH1 is the first detector of the LHCb RICH system. It is installed behind the VELO, and it covers an angular acceptance from 25 to 300 mrad in the magnet bending plane and from 25 to 250 mrad in the vertical direction. Alone, it provides PID in the momentum range between 2.6 and 60 GeV/ c using a C₄F₁₀ gas Cherenkov radiator. The photon detector planes, populated with multianode photomultiplier tubes (MaPMTs), are located above and below the beam pipe, where the residual magnetic field is minimal [4].

The Upstream Tracker (UT) is located between the RICH1 detector and the dipole magnet. The UT detector comprises four planes of silicon detectors organized in two stations, with a circular hole in the middle to provide clearance for the beam pipe. The UT tracks are combined with the VELO tracks to give a first determination of the track momentum p with a moderate precision of $\sim 15\%$ [4].

The LHCb dipole magnet has been maintained unchanged with respect to Run 1-2. It provides a vertical magnetic field with a bending power of $\simeq 4\text{Tm}$, and it consists of two identical saddle-shaped coils which are mounted symmetrically inside a window-frame yoke. During data taking, the magnet polarity is reversed every few weeks to collect data sets of similar size with the two field configurations [4].

The Scintillating Fibre (SciFi) tracker is located behind the magnet and is designed for the tracking of charged particles exiting the magnet and for their momentum measurement. The detector technology is based on plastic scintillating fibers, 250 μm in diameter, and arranged in multilayered honeycomb carbon-fiber mats. In total, there are 12 detection planes arranged in 3 stations (T1, T2, T3) with four mats each. A thin mirror is glued to the inner end of the fiber to reflect light back to the readout side, where it is detected with a silicon photomultiplier (SiPM) [4].

RICH2 is placed downstream of the dipole magnet, covering an angular acceptance from 15 to 120 mrad in the magnet bending plane and 15 to 100 mrad in the vertical direction. It is designed to provide PID for higher momentum particles, between 15 and 100 GeV/ c , with a CF₄ gas radiator and detector planes on the sides. RICH2 uses the same 1-inch type of MaPMTs of the RICH1 in the high occupancy region, but in the outer region, it uses a 2-inch variant of the device instead [4].

The layouts of both, the electromagnetic calorimeter (ECAL) and the hadronic calorimeter (HCAL) remain unchanged for the upgrade. The ECAL is discussed in more detail in chapter 2.4. The HCAL is a sampling tile calorimeter with a thickness

of 5.6 interaction lengths. This thickness is insufficient for a full hadronic shower containment, but regardless, it complied with the trigger requirements for Run 1 and 2. The sampling structure consists of staggered iron and plastic scintillator tiles mounted parallel to the beam axis to enhance the light collection. From there, the light is transmitted to the PMTs with wavelength shifting (WLS) fibers [4].

The muon system covers a volume of 385 m^2 and is the last sub-detector of the LHCb experiment. It has four stations (M2 to M5) comprising 1104 multi-wire proportional chambers (MWPC) interleaved with 80 cm thick iron absorbers. Due to the increase in luminosity after Run 2, the particle flux in the innermost region of station M2 is expected to be very high, resulting in an unevenly distributed efficiency drop of about 7%, on average, in the region closest to the beam pipe. In order to reduce the inefficiencies, additional shielding has been placed around the beam pipe before the M2 station [4].

1.1.2 Upgrade II of the LHCb experiment

Upgrade II will bring further improvements to the detector of the LHCb experiment. These are needed so the experiment can start data taking after LS4 in 2032 and collect a minimum of 300 fb^{-1} at maximum luminosity of $1.5 \times 10^{34} \text{ cm}^{-2} \text{ s}^{-1}$ [5].

Tracking

At luminosity of $1.5 \times 10^{34} \text{ cm}^{-2} \text{ s}^{-1}$ around 2000 charged particles will be produced per bunch crossing within the LHCb acceptance. For this reason, it is foreseen to modify the existing tracking sub-detectors to increase the granularity, reduce the amount of material in the detector, and exploit the use of precision timing. The new Vertex Locator (VELO) will be based, as in the current detector, on high-granularity pixels operated in a vacuum in close proximity to the LHC beams. To cope with the expected large density of primary interaction along the beam axis, the VELO will have to include timing information with a precision of better than 50 ps to each hit, leading to a track time stamp resolution of approximately 20 ps. The tracking system installed behind the VELO will keep the design of the current detector and consist of a tracking detector located upstream (UT) and three tracking stations (MT) located downstream of the magnet. Together with the VELO, these stations will provide a high-precision momentum measurement and measure the track direction of the charged particles. The tracking detectors will have increased granularity and will be more radiation tolerant compared to their predecessors [5].

Particle identification

High-performing particle identification (PID) is essential for almost all precision flavor measurements. A common theme for PID detectors at LHCb will be improved granularity and, for some, fast timing on the order of a few tens of picoseconds. The RICH system will again consist of RICH1, located upstream and providing PID in the low momentum range, and RICH2, located downstream and covering the high momentum range. To cope with the increased track multiplicity, the RICH system will have to use new photodetectors of higher granularity instead of multianode photomultipliers. Fast timing capability is an additional essential attribute, and a further improvement of the Cherenkov angle resolution by at least a factor of three will be necessary. The LHCb physics program will be extended by the addition of a TORCH detector. This sub-detector measures time-of-flight through the detection

of internally reflected Cherenkov light produced in a thin (~ 1 cm) quartz plane. A time resolution of a few tens of picoseconds per photon would allow for a substantial improvement of kaon and proton identification at low momenta. A redesigned ECAL, discussed more in detail in chapter 3, will have to withstand severe radiation doses up to 1 MGy in the innermost region. Secondly, the operation at a high luminosity will lead to overlapping showers and a corresponding degradation in energy resolution and shower finding efficiency. To address this challenge, the Moliere radius and cell size of the inner ECAL region will have to be reduced. Lastly, to reduce an unacceptably large combinatorial background and to associate the candidates to individual proton-proton (pp) interactions in the bunch crossing, fast-timing information on the order of a few tens of picoseconds will be essential. At Upgrade II, extra shielding will be required in front of the muon detector to suppress the flux of punch-throughs to a more manageable level. This can be achieved by replacing the HCAL, as it is no longer needed, with up to 1.7 m of iron, which would provide an additional four interaction lengths compared to the current situation. For the muon system, new detectors will be needed in the innermost region of all stations, with a design possessing both high granularity and high rate capability [5].

Trigger and data processing

Operating at the luminosity of $1.5 \times 10^{34} \text{ cm}^{-2} \text{ s}^{-1}$, the LHCb detector is expected to produce up to 200 Tb of data per second, which will have to be processed in real-time and reduced by around four orders of magnitude before being sent to permanent storage. The Upgrade II data processing will be based around pile-up suppression, in which detector hits not associated with the individual pp interaction of interest are discarded as early as possible in the processing chain. In particular, the timing information will play a crucial role in the fast separation of reconstructed objects according to the pp interaction that produced them. The successor of the full software trigger, currently used in Run 3, will again be implemented on a processor farm and supplemented with GPU or FPGA accelerators [5].

2. Calorimetry in particle physics

Calorimetry is a widespread detection principle in particle physics. The method was originally designed to study cosmic-ray phenomena but was later adopted and further developed for accelerator-based particle physics experiments, primarily to measure the energy of electrons, photons, and hadrons. Traditionally, calorimeters consist of blocks of instrumented material in which particles are fully absorbed, and their energy is converted into a measurable quantity, such as scintillation light [6].

Calorimeters can be broadly divided into electromagnetic calorimeters, used mainly to measure the energy of electrons and photons through their electromagnetic interactions (e.g., bremsstrahlung, pair production), and hadronic calorimeters, used to measure mainly the energy of hadrons through their strong and electromagnetic interactions. They can be further classified based on their construction technique into sampling calorimeters and homogeneous calorimeters [6, 7, 8].

Sampling calorimeters consist of alternating layers of passive and active medium. The passive layer is a dense absorber with large atomic number Z , such as lead, iron or copper, to maximize the stopping power. The active layer samples the deposited energy after the incident particle generates a shower of charged particles [7, 9].

Homogeneous calorimeters, on the other hand, are built of a single material type that performs both tasks, energy degradation and signal generation [6].

Calorimetry is not the only method that allows energy measurements in high energy physics, but it remains an attractive choice in this field for various reasons [6, 8]:

- Contrary to magnetic spectrometers, in which the momentum resolution deteriorates linearly with the particle momentum, in calorimeters the energy resolution usually improves with the energy of the incident particle E as $1/\sqrt{E}$.
- In contrast with magnetic spectrometers, calorimeters are sensitive to electromagnetic and strong particle interactions. They can even allow indirect detection of neutrinos through a measurement of the event's missing energy.
- Although in the past calorimeters were often perceived as devices solely for energy measurement, they can be used to determine shower position and direction, for particle identification, and to provide a precise timing measurement.
- Calorimeters can be relatively compact because the shower length increases logarithmically with particle energy. Consequently, to contain the shower, the thickness of a calorimeter only needs to increase logarithmically with the particle energy. In contrast, for a fixed momentum resolution, the bending

power BL^2 of a magnetic spectrometer (where B is the magnetic field and L is the length) must increase linearly with the particle momentum.

- Calorimeters can provide a precise measurement of the particle arrival time. This information is often crucial for the experiment as it helps mitigate event pileup and contributes to background suppression in some physics channels.

2.1 Passage of radiation through matter

When an energetic particle passes through matter, it will deposit some of its energy along the way. The dominant interaction governing energy losses varies based on the particle type and its energy, as well as the properties of the material through which it propagates. Taking this into consideration, electromagnetic and hadronic calorimeters are built differently, and both have their unique challenges.

2.1.1 Energy loss of electrons and positrons

Like heavy charged particles, electrons and positrons suffer a collisional energy loss when passing through matter by numerous inelastic collisions with the orbital electrons of the medium. However, because of their small mass, an additional energy loss mechanism emerges from scattering in the electric field of a nucleus. This process is known as *bremstrahlung* and is classically understood as radiation arising from the acceleration of an electron (or positron) as it deviates from its straight-line course by the electric interaction with the nucleus. At energies of a few MeV or less, this process is still a relatively small factor. It becomes comparable to or greater than the collision-ionization loss at energies above the *critical energy* (ϵ_c), which depends on the material type and can be empirically calculated as [7, 10]:

$$\epsilon_c = \frac{610 \text{ MeV}}{Z + 1.24} \quad \text{for solids and liquids} \quad (2.1)$$

$$\epsilon_c = \frac{710 \text{ MeV}}{Z + 0.92} \quad \text{for gases} \quad (2.2)$$

Therefore, the total energy loss of electrons and positrons includes two parts [10]:

$$\left(\frac{dE}{dx}\right)_{\text{tot}} = \left(\frac{dE}{dx}\right)_{\text{rad}} + \left(\frac{dE}{dx}\right)_{\text{coll}} \quad (2.3)$$

Energy loss by collision: Bethe-Bloch equation

While the basic mechanism of collision loss for heavy charged particles is also valid for electrons and positrons, the Bethe-Bloch formula must be modified somewhat for two reasons. First, due to their small mass, the assumption that the incident particle remains undeflected during the collision process is invalid. The second is that, for electrons, the collisions are between identical particles. Hence, the calculation must account for their indistinguishability. With these two modifications to the Bethe-Bloch equation, the correct equation to describe the collision loss part of the total energy loss of electrons and positrons is as follows [10]:

$$-\left(\frac{dE}{dx}\right) = 2\pi N_a r_e^2 m_e c^2 \rho \frac{Z}{A} \frac{1}{\beta^2} \left[\ln \frac{\tau^2(\tau + 2)}{2(I/m_e c^2)^2} + F(\tau) - \delta - 2\frac{C}{Z} \right] \quad (2.4)$$

where:

2.1. Passage of radiation through matter

N_a : Avogadro number = $6.022 \times 10^{23} \text{ mol}^{-1}$	A : atomic weight of absorbing material
r_e : classical electron radius = $2.817 \times 10^{-13} \text{ cm}$	β : v/c of incident particle
m_e : electron mass = 511 keV	τ : kinetic energy of particle in units of $m_e c^2$
ρ : density of absorbing material	I : mean excitation potential
Z : atomic number of absorbing material	δ : density correction
	C : shell correction

$F(\tau)$ takes two forms, depending on whether the particle is an electron or a positron:

$$F(\tau) = 1 - \beta^2 + \frac{\tau^2 - (2r + 1) \ln 2}{(\tau + 1)^2} \quad \text{for } e^- \quad (2.5)$$

$$F(\tau) = 2 \ln 2 - \frac{\beta^2}{12} \left(23 + \frac{14}{\tau + 2} + \frac{10}{(\tau + 2)^2} + \frac{4}{(\tau + 2)^3} \right) \quad \text{for } e^+ \quad (2.6)$$

Energy loss by radiation: Bremsstrahlung

As shown in figure 2.1, at energies below a few hundred GeV, only electrons and positrons have a substantial contribution of bremsstrahlung to the energy loss [10].

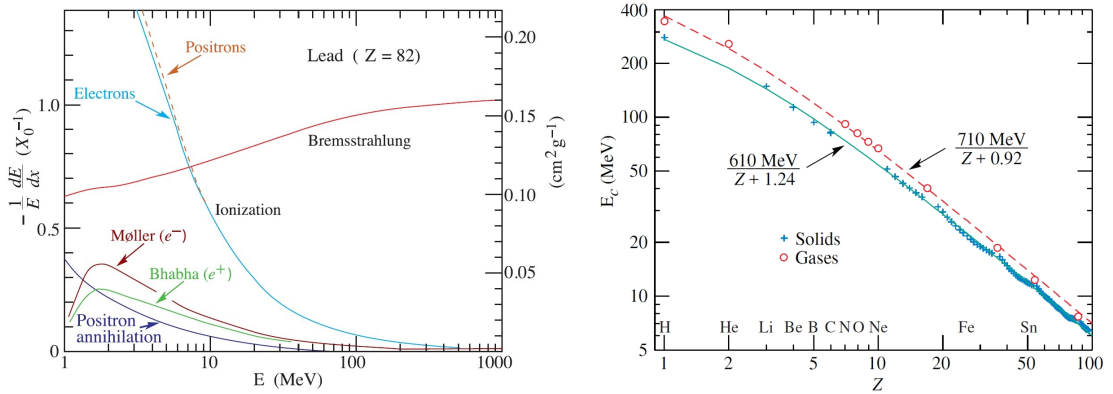


Figure 2.1: (a) Fractional energy loss per radiation length in lead as a function of electron or positron energy [11]. (b) Electron critical energy for some elements [11].

The emission probability, in fact, varies as the inverse square of particle mass [10]:

$$\sigma \propto (e^2 m c^2)^2 \quad (2.7)$$

As an illustration, the radiation loss by muons ($m = 106 \text{ MeV}$), the next lightest particle, is approximately 40,000 times smaller than that for electrons.

Instead of the critical energy, a similar quantity known as the *radiation length* (X_0) is more often used. It is defined as the average distance over which the electrons' energy is reduced by the factor $1/e$ due to radiation loss only. Table 2.1 shows values of critical energies and radiation lengths of some common detector materials [10].

Table 2.1: Critical energies and radiation lengths of some materials [10, 11].

material	Pb	W	Fe	Cu	NaI	H ₂ O	Polystyrene
ϵ_c [MeV]	9.51	7.97	27.4	24.8	17.4	92.0	109
X_0 [cm]	0.56	0.35	8.90	1.76	2.59	36.1	42.9

2.1.2 Interactions of photons with matter

The behavior of photons (in this section, high-energy photons) in matter is substantially different from that of charged particles. Since photons lack electric charge, they do not undergo the numerous inelastic collisions inherent to charged particles. Instead, the main interactions of high-energy photons in matter are [10]:

1. Photoelectric effect
2. Compton scattering
3. Pair production

The cross-section for these interactions varies with photon energy, as shown in figure 2.2. Consequently, each interaction dominates within a certain energy regime. The specific energy thresholds at which a particular interaction becomes dominant depend on the atomic number Z of the material through which the photons propagate. Although, as a rule of thumb, the photoelectric effect dominates in the keV range, Compton scattering is prevalent in the energy range between 0.5 to 10 MeV, and pair production becomes dominant above a few tens of MeV.

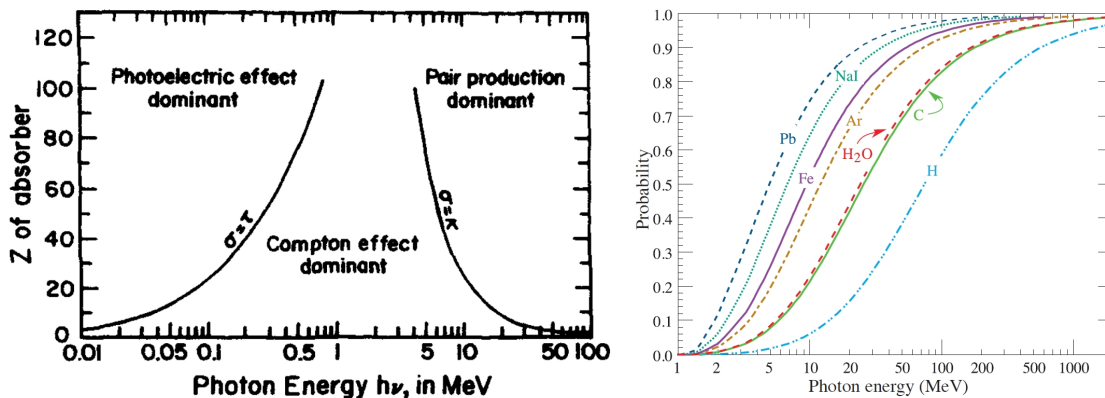


Figure 2.2: (a) Relative importance of the three major types of photon interactions. The curves show values of Z and E_γ for which two types of effects are equal [12]. (b) Probability that a photon interaction results in conversion to an e^-e^+ pair [11].

In collider-based particle physics, the energies of photons entering a calorimeter normally range from at least a few hundred MeV to several hundred GeV, making pair production the dominant interaction. This process involves the transformation of a photon into an electron-positron pair. In order to conserve momentum, this can only occur in the presence of a third body, usually a nucleus. Moreover, to create the pair, the photon must have at least an energy of 1.022 MeV [10].

2.1.3 Physics of an electromagnetic cascade

In spite of the apparently complex phenomenology of shower development in a material, electrons and photons interact with matter via a few well-understood quantum electrodynamics (QED) processes, and the main shower features can be parametrized with simple empirical functions [6].

The average energy lost by electrons in lead and the dominant photon interactions are shown as a function of energy in figures 2.1 and 2.2, respectively. Like this, two main regimes can be identified. For energies larger than ~ 10 MeV, the main source of electron energy loss is bremsstrahlung. In this energy range, photon interactions produce mainly electron-positron pairs. For energies above 1 GeV, both mentioned processes become roughly energy-independent. At low energies, electrons lose their energy mainly through collisions with the atoms and molecules of the material, thus giving rise to ionization and thermal excitation. Photons lose their energy through Compton scattering or convert into an electron through the photoelectric effect [6].

As a consequence, electrons and photons of sufficiently high energy (≥ 1 GeV) incident on a block of material produce secondary photons by bremsstrahlung or secondary electrons and positrons by pair production. These secondary particles, in turn, undergo the same processes, thereby initiating a cascade (or shower) of particles. The cascade continues until the energy of the pair-produced electrons and positrons drops below the critical energy. At this point, the newly produced particles will primarily lose their energy through ionization and excitation rather than bremsstrahlung emission, effectively stopping the cascade [6, 10].

The main features of electromagnetic showers, such as their longitudinal and lateral sizes can be described in terms of one parameter, the radiation length X_0 , which was introduced in chapter 2.1.1. An approximation of the radiation length can be obtained using the following formula [6, 11]:

$$X_0 \text{ (g/cm}^2\text{)} \simeq \frac{716 \cdot \text{ g cm}^{-2} A}{Z(Z+1) \ln(287/\sqrt{Z})} \quad (2.8)$$

where Z and A are the atomic number and weight of the material, respectively.

The physical scale over which a shower develops is similar for incident electrons and photons and is independent of the material type if expressed in terms of radiation length. Consequently, electromagnetic showers can be described universally using simple functions of X_0 [6].

Shower maximum and longitudinal shower containment

The shower maximum, which refers to the depth at which the largest number of secondary particles is produced, is approximately located at [6]:

$$t_{\max} \simeq \ln \frac{E_0}{\epsilon_c} + t_0 \quad (2.9)$$

where t_{\max} is measured in radiation lengths, E_0 is the incident particle energy, and $t_0 = -0.5$ for electrons (and positrons) and $t_0 = +0.5$ for photons. The formula shows a logarithmic dependence of the shower length (and with that, the detector

thickness needed to absorb a shower) on the incident particle energy. The calorimeter thickness containing 95% of the shower energy is approximately given by [6]:

$$t_{95\%} \simeq t_{\max} + 0.08 \cdot Z + 9.6 \quad (2.10)$$

where t_{\max} and $t_{95\%}$ are measured in radiation lengths. In calorimeters with a thickness of $\sim 25 X_0$, the longitudinal shower leakage beyond the end of the active detector is much less than 1% up to incident electron energies of ~ 300 GeV [6].

Molière radius

As the cascade develops, its lateral dimensions expand due to multiple scattering of electrons and positrons in the direction away from the shower axis. Additional contributions arise from the bremsstrahlung photons emitted by these particles and the finite opening angle between electron and positron in pair production [6, 10].

A measurement of the transverse size, integrated over the full shower depth, is given by the Molière radius R_M , which can be approximated by [6]:

$$R_M \text{ (g/cm}^2\text{)} \simeq 21 \cdot \text{MeV} \frac{X_0}{\epsilon_c(\text{MeV})} \quad (2.11)$$

It represents the average lateral deflection of electrons at the critical energy after traversing one radiation length. On average, around 90% of the shower energy is contained in a cylinder of radius $\sim 1 R_M$. In most calorimeters, R_M is by design limited to a few centimeters, resulting in narrow electromagnetic showers. Figure 2.3 shows a simulation of the fraction of the energy shower deposits in the material at different depths and distances from the shower axis.

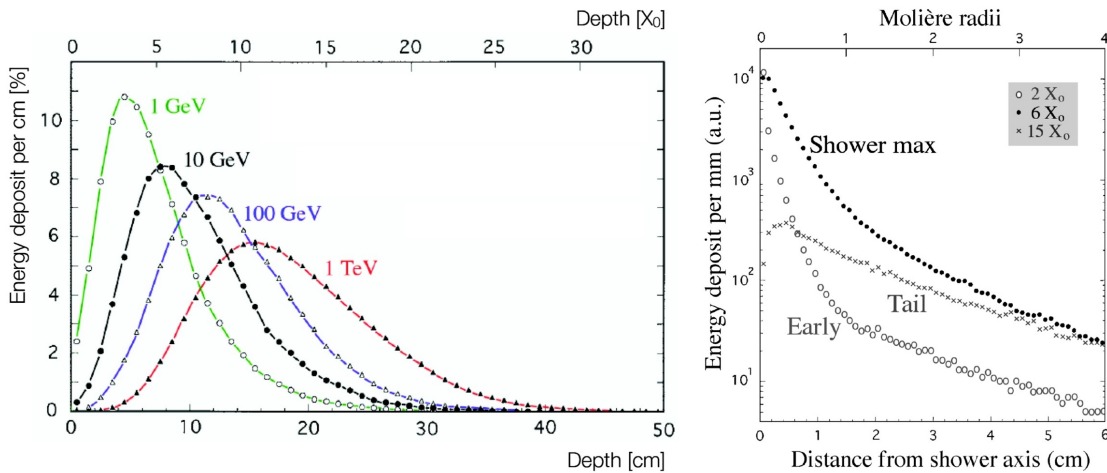


Figure 2.3: (a) Simulated longitudinal shower profiles in PbWO_4 for various electron energies as a function of the material thickness [9]. (b) Radial distributions of the energy deposited by 10 GeV electron showers in copper at three different depths [9].

2.2 Scintillation-based sampling calorimeters

Sampling calorimeters are classified, by the type of active medium, into scintillation calorimeters, gas calorimeters, solid-state calorimeters, and liquid calorimeters. In

scintillation-based sampling calorimeters, the signal is collected in the form of light, before it is converted into electric charge. In contrast, gas, solid-state, and liquid calorimeters collect the signal directly in the form of electric charge [6].

A large number of sampling calorimeters use organic (plastic) scintillators arranged in fibers or plates. This choice offers detectors which [6]:

- are relatively cheap,
- can be built in a large variety of geometries,
- can be easily segmented,
- have a fast response and an acceptable light yield.

Primary factors that restrict the long-term optimal operation of sampling calorimeters based on organic fibers include aging and the effects caused by radiation damage. In such cases, the organic fibers can be replaced with more expensive scintillating crystals, for example, Cerium-doped $\text{Gd}_3\text{Al}_2\text{Ga}_3\text{O}_{12}$ (GAGG:Ce), included in table 2.2, which offers similar performance but can withstand higher radiation doses [13].

2.2.1 Operation of scintillation detectors

Scintillation-based detectors are not exclusive to calorimeters as they find broader applications in radiation detection. These detectors convert radiation into scintillation light which is subsequently converted into an electric pulse. Traditionally, they consist of two primary components: a scintillator and a photodetector.

Scintillators

Scintillation is a type of luminescence induced by ionizing radiation in dielectric media. When ionization excites a material containing luminescence centers, the following will relax through photon emission. Such materials are known as *scintillators* and can be broadly divided into two groups: inorganic and organic scintillators [9].

Table 2.2: A few selected properties of common inorganic scintillators [7, 14].

material	NaI:Tl	GAGG	BGO	PbWO ₄
density [g/cm ³]	3.67	6.67	7.13	8.28
radiation length	2.60 cm	1.61 cm	1.11 cm	0.89 cm
emission maximum	415 nm	520 nm	480 nm	420(25) nm
decay time	0.23 μs	36, 122 ns	0.3 μs	10, 30 ns
light yield [ph/MeV]	37700	26280, 9720	8200	100, 31
radiation hardness	10 Gy	$> 10^6$ Gy	10^{2-3} Gy	$> 10^5$ Gy

Inorganic scintillators are known for their high stopping power and good light yield, and some typical values are shown in table 2.2. Scintillators can have multiple decay channels, resulting in a set of distinct decay times. Applications that require precise

timing, typically prefer scintillators that have shorter decay times.

In comparison to inorganic scintillators, organic scintillators have a lower density, which affects their stopping power. Nevertheless, they are generally cheaper and often exhibit shorter decay times and thereby have better timing capabilities.

Photodetectors

In most photodetectors, the detection of photons proceeds in three steps. First, a primary photoelectron or electron-hole pair is created by an incident photon via the photoelectric or photoconductive effect. In the second step, the number of electrons is increased to a detectable level through electron multiplication, so that, in the third step, the electrons produce an electric signal. The three steps are best illustrated in the example of the photomultiplier tube (PMT) shown in figure 2.4, a common light sensor with a structure of electrodes enclosed in an evacuated glass vessel [7].

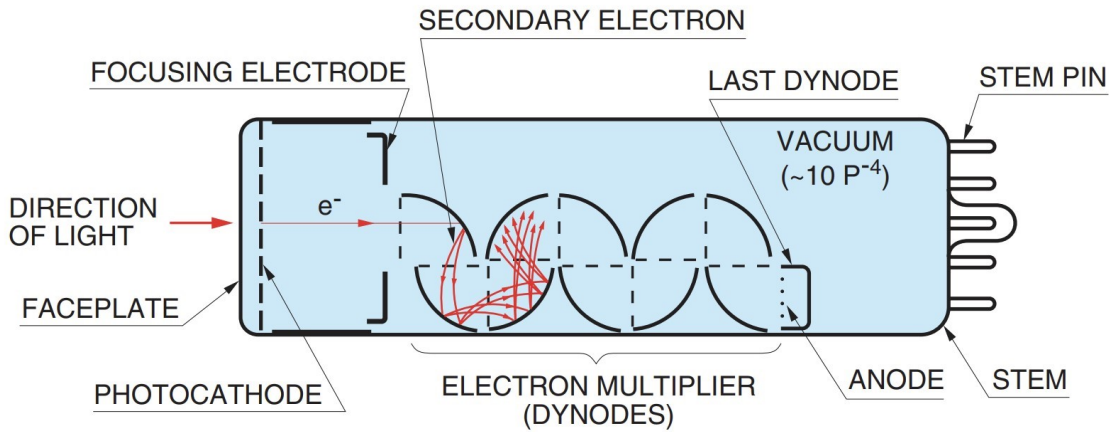


Figure 2.4: Schematics of a transmission-type photomultiplier tube [15].

In a PMT, a photon hits a semitransparent photocathode and kicks out an electron. The exiting photoelectron enters the electric field of the first dynode and starts the multiplication process. The dynodes serve as an electron multiplier chain: electrons accelerate in the electric field, strike the next dynode, and release more electrons. After several amplification stages, the cloud of electrons hits the last electrode, the anode, which collects the electrons and produces an electric signal [7].

Photomultiplier tubes come in different geometries, more specifically, they can be classified by the dynode type and the arrangement of the dynodes into linear-focused type, circular-cage type, etc. A special PMT type is the metal channel dynode (MCD) PMT. Its dynode structure consists of extremely thin and precisely stacked electrodes. Since each dynode is in close proximity to one other, this group of PMTs exhibits good timing properties and is less affected by strong magnetic fields [16].

2.3 Energy resolution of a calorimeter

The energy measurement principle used for calorimeters assumes a proportional correlation between the energy deposited inside the calorimeter and the energy of an incident particle E_0 . When a shower develops, the total track length of the shower

T_0 is defined as the sum of all ionization tracks due to secondary charged particles in the electromagnetic cascade. For a homogeneous calorimeter the formula:

$$T_0 \text{ (g/cm}^2\text{)} \propto X_0 \frac{E_0}{\epsilon_c} \quad (2.12)$$

shows that a measurement of the signal produced by the charged tracks of the cascade provides a measurement of the original particle energy [6].

What limits the energy resolution of an ideal calorimeter are fluctuations of the track length T_0 . The shower development follows a stochastic process governed by Poisson statistics. The fractional energy resolution can be derived from purely statistical arguments and presented as [6]:

$$\frac{\sigma_E}{E} \propto \frac{1}{\sqrt{T_0}} \propto \frac{1}{\sqrt{E_0}} \quad (2.13)$$

The energy resolution of a realistic calorimeter is further limited by contributions coming from instrumental effects, such as inefficiencies in the signal collection, material inhomogeneities, and mechanical constraints (e.g., finite calorimeter thickness). This gives us a general formula for energy resolution of a realistic calorimeter [6]:

$$\frac{\sigma_E}{E} = \frac{a}{\sqrt{E}} \oplus \frac{b}{E} \oplus c \quad (2.14)$$

where the symbol \oplus means a sum in quadrature. The first term on the right-hand side is the stochastic term and includes the intrinsic shower fluctuations described with equation 2.13. The second term is the noise term and the third term is the constant term. The dominating term for the energy resolution depends on the energy of the incident particles. This effect plays an important role during the calorimeter design because different techniques can optimize different terms in the equation 2.14 to maximize the calorimeter performance for the expected operating energy range.

Stochastic term

In homogeneous calorimeters, the intrinsic fluctuations are small because the same material acts both as an absorber and active volume. Therefore, the energy deposited within the calorimeter is always seen by the active medium and it fluctuates little from event to event. In most cases, the intrinsic energy resolution of homogeneous calorimeters can surpass the statistically expected value, thanks to the *Fano factor*. The Fano factor has values ≤ 1 , and it includes the effects of various fundamental processes that can lead to an energy transfer in the detector. It is experimentally determined and is an intrinsic constant of the detecting medium [6, 10].

In contrast, sampling calorimeters consist of alternating layers of the passive and active medium, which leads to greater fluctuations of the energy deposited inside the active medium on an event-to-event basis. These fluctuations, commonly referred to as *sampling fluctuations*, set the most significant limitation to the energy resolution of sampling calorimeters, and are due to variations in the number of charged particles N_{ch} that cross through the active layer. This number is proportional to [6]:

$$N_{ch} \propto \frac{E_0}{t} \quad (2.15)$$

where t is the thickness of absorber layers in radiation lengths. Inserting equation 2.15 into equation 2.13, the stochastic term can be expressed as [6]:

$$\frac{\sigma_E}{E} \propto \frac{1}{\sqrt{N_{\text{ch}}}} \propto \sqrt{\frac{t}{E_0(\text{GeV})}} \quad (2.16)$$

By reducing the thickness of the absorber layers, the deposited energy can be sampled more frequently, resulting in improved energy resolution. In practice, however, it is not feasible to make the absorber layers thin enough to reach a few percent of the radiation length. As a result, achieving resolutions comparable to those typically found in homogeneous calorimeters becomes challenging.

Noise term

The noise term includes contributions from the readout circuit and electronics, and its magnitude is predominantly influenced by the detection technique. In scintillation-based calorimeters, the noise term stays relatively low if an amplifying photodetector, such as a photomultiplier tube (PMT), detects the scintillation light. In contrast, calorimeters that collect the signal directly in the form of electric charge typically achieve a worse signal-to-noise ratio even with the use of a pre-amplifier in the readout chain. Nonetheless, both detection techniques are limited by the following relation, which shows that the equivalent noise charge σ_Q increases at higher sampling rates [6]:

$$\sigma_Q = \sqrt{4k_B R T \Delta f} \quad (2.17)$$

where k_B is the Boltzmann constant, T the temperature, R the equivalent noise resistance, and Δf the sampling bandwidth.

Another parameter that affects the stochastic term and the noise term in the energy resolution of sampling calorimeters is the so-called *sampling fraction* f_{samp} [6]:

$$f_{\text{samp}} = \frac{E_{\text{mip}}(\text{active})}{E_{\text{mip}}(\text{active}) + E_{\text{mip}}(\text{absorber})} \quad (2.18)$$

where $E_{\text{mip}}(\text{active})$ and $E_{\text{mip}}(\text{absorber})$ represent the energies deposited by an incident minimum-ionizing particle (MIP) in the active part and in the absorber part of the detector, respectively. Increasing the sampling fraction makes the signal in the active medium larger, which in turn leads to a higher signal-to-noise ratio.

Constant term

The constant term, as the name suggests, remains independent of the particle's energy. It manifests due to instrumental effects such as inefficiencies in signal collection, material inhomogeneities, and mechanical constraints. These effects cause variations of the calorimeter response with the particle impact point on the detector and give rise to response non-uniformities. Response non-uniformity introduces additional smearing to the measured energy over larger instrumented areas. A common source of non-uniformities are irregularities of the absorber and active layer shapes, non-hermetic coverage, such as cracks and dead regions inside the calorimeter volume, variations in response due to temperature gradients, and effects caused by radiation damage and detector aging. If these effects exhibit periodic behavior,

they can be partially corrected using specific calibration techniques. However, in the case of randomly distributed ones, the correction becomes more difficult [6].

Since the constant term typically becomes the dominant factor influencing the energy resolution of calorimeters in the higher energy range, it is essential to keep it at a percent level or lower. This is even more significant for homogeneous calorimeters due to their intrinsically low values of stochastic and noise term [6].

Additional contributions

Additional contributions to the energy resolution not explicitly mentioned in the sections above come from the constraints to which a calorimeter is subjected when integrated into a big experiment. These include, but are not only limited to longitudinal leakage, lateral leakage, and upstream energy losses [6].

2.4 Electromagnetic calorimeter of the LHCb

The LHCb electromagnetic calorimeter (LHCb ECAL) uses the Shashlik technology, a stack of alternating tiles of absorber and scintillator, penetrated by wavelength shifting (WLS) fibers running perpendicular to the tiles, collecting the scintillation light and guiding it to a light detector. An ECAL module is a sampling scintillator/lead structure readout by Kuraray [17] Y-11(250) plastic wavelength shifting fibers, emitting in green, connected to a Hamamatsu [16] R7899-20 PMT, which is a head-on-type photomultiplier tube with a linear-focused dynode structure. This alternating calorimeter structure consists of 2 mm thick lead plates, 0.12 mm thin reflecting TYVEK paper sheets, and 4 mm thick plastic scintillator tiles [4, 18].

The decision to build the ECAL in this technology was made taking into account modest energy resolution, fast time response, acceptable radiation resistance, and reliability of the shashlik technology, as well as the experience accumulated by other experiments. The shashlik module length corresponds to $25 X_0$, and the Moliere radius of the stack is 3.5 cm. The energy resolution of a given cell, measured with a test electron beam, was shown to be [4]:

$$\frac{\sigma_E}{E} = \frac{(9.0 \pm 0.5)\%}{\sqrt{E}} \oplus (0.8 \pm 0.2)\% \oplus \frac{0.003}{E \sin \theta} \quad (2.19)$$

where E is the particle energy in GeV and θ is the angle between the beam axis and the line from the LHCb interaction point to the centre of the ECAL cell.

The ECAL front surface is about 12.5 m from the interaction point. The square cell sizes are shown in figure 2.5, for the inner, middle, and outer regions are 40.4 mm, 60.6 mm, and 121.2 mm, respectively. A geometry, as shown in figure 2.6, ensures a roughly uniform particle rate per cell. In total, the ECAL consists of 3312 modules (6016 channels), with 176 inner type modules, 448 middle type modules, and 2688 outer type modules. The outer dimensions of the ECAL match projectively those of the tracking system: $\theta_x < 300$ mrad and $\theta_y < 250$ mrad, while the inner angular acceptance of ECAL is limited to $\theta_{x,y} > 25$ mrad around the beam pipe, where θ_x and θ_y are the polar angles in the xz and yz planes in the LHCb reference frame [4].

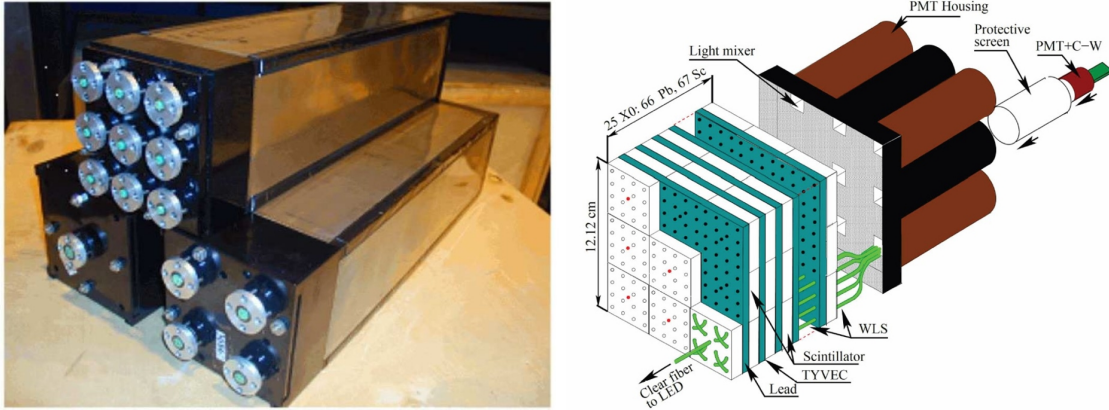


Figure 2.5: (a) Going in the clockwise direction from the top: inner, middle and outer type ECAL modules [18]. (b) Schematic of an inner type shashlik module [4].

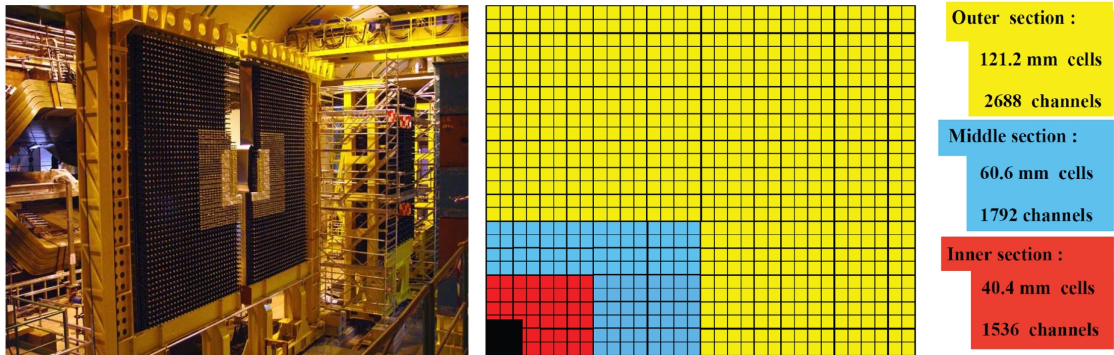


Figure 2.6: (a) Downstream view of the (not completely closed) LHCb ECAL [18]. (b) Lateral segmentation of the ECAL. One quarter of the detector is shown [4].

3. SpaCal with tungsten absorber

At the end of 2025, there will be a Long Shutdown 3 (LS3) of the LHC, which will last for three years [19]. During that period, many experiments at LHC, including the LHCb experiment, will use this downtime to service and upgrade their detectors.

Given preparation for Run 4 and the after-coming Long Shutdown 4 (LS4), the LHCb ECAL will have to undergo a major reconstruction. The goal of collecting an integrated luminosity of 300 fb^{-1} in Upgrade Phase II comes with a cost. It implies that the calorimeter must be capable of sustaining integrated radiation doses of up to 1 MGy in the innermost region and deal with much higher occupancy, as shown in figure 3.1. The radiation limit of the current Shaslik technology is around 40 kGy and operation above this limit would mean significant losses in the performance of the calorimeter, in particular, its energy resolution [20, 21, 22].

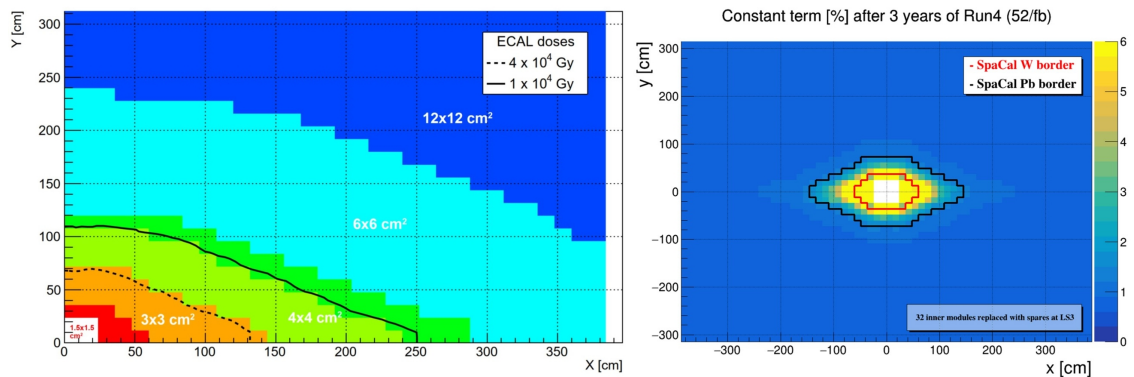


Figure 3.1: (a) ECAL regions after Upgrade II. Colors represent different cell sizes, and black solid and dashed lines show radiation boundaries [21]. (b) Expected constant term of energy resolution in percentage after 3 years of Run 4 (collecting an integrated luminosity of 52/fb) if the ECAL was not upgraded during LS3 [22].

The proposed solution is to replace the current Shaslik modules in the inner two regions with the new Spaghetti Calorimeter (SpaCal) modules built in three different technologies. These are the requirements the new ECAL has to meet for LS3 [22]:

- **Rapidity coverage.** To detect rare physics processes, the maximum possible acceptance has to match that of the charged particle spectrometer.
- **Energy resolution** of $(\sigma_E/E) = 10\%/\sqrt{E} \oplus 1\%$ in the energy range from a few to a few hundred GeV. This is crucial for reliable reconstruction of π_0 and η mesons in presence of high combinatorial background, and for electron identification. Having a small constant term in the energy resolution is particularly important for the studies of radiative B decays.

- **Response linearity** of $\leq 1\%$ at energies relevant to the physics programme.
- **Moliere radius** similar to the cell size, and short **radiation length** to ensure a compact calorimeter design with a thickness corresponding to at least $25 X_0$.
- **High granularity** as shown in figure 3.2 is needed for electron identification, two-shower separation, and accurate energy and position resolution.

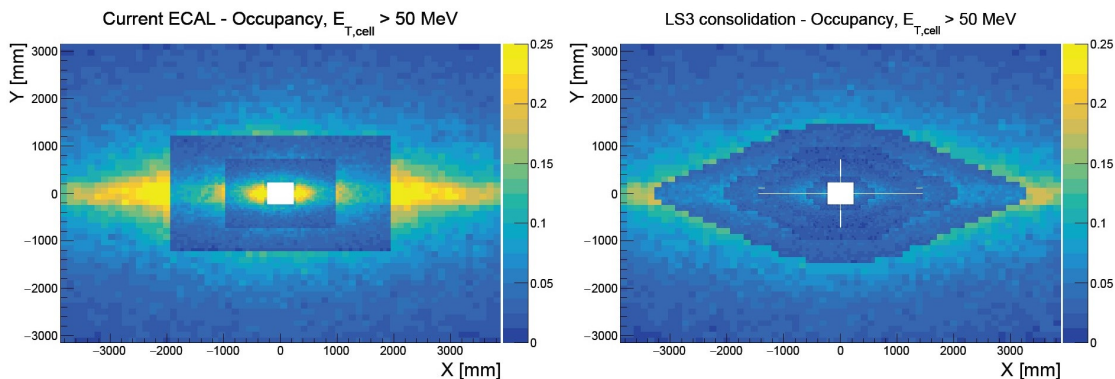


Figure 3.2: (a) Occupancy per cell assuming a luminosity of $2 \times 10^{33} \text{ cm}^{-2} \text{ s}^{-1}$ in the current ECAL [22]. (b) Expected occupancy per cell in the ECAL configuration to be installed during LS3 [22].

In addition to the LS3 requirements mentioned above, for LS4, the ECAL will have to feature **radiation hardness** and withstand radiation doses of up to 1 MGy and neutron doses of $\leq 6 \times 10^{15} \text{ 1 MeV neq/cm}^2$ in the innermost part. Another requirement will be the inclusion of **fast time response** with time resolution $O(10\text{ps})$.

3.1 SpaCal technologies

A "spaghetti calorimeter (SpaCal)" is a sampling calorimeter where scintillating fibers are inserted inside a dense absorber. The PicoCal group chose this technology to replace the current Shaslik modules in the innermost part of the ECAL because it satisfies the upgrade requirements. After the LS3 consolidation, the region closest to the beam pipe will host SpaCal (WPoly) modules with tungsten absorber and polystyrene scintillating fibers, and the next region, SpaCal (PbPoly) modules with lead absorber and polystyrene scintillating fibers. The design cell sizes are $2 \times 2 \text{ cm}^2$ for the SpaCal WPoly modules and $3 \times 3 \text{ cm}^2$ for the SpaCal PbPoly modules [22].

During LS4, ECAL will undergo further modifications, as summarized in table 3.1. A longitudinal segmentation will be introduced in the SpaCal PbPoly modules. Modules will now consist of two sections (8 cm + 21 cm) separated by a mirror and read out from both sides. The same will apply to the modules with the tungsten absorber, but additionally, the polystyrene scintillating fibers will be replaced by GAGG crystal scintillating fibers. The replacement of the fibers is necessary to increase the radiation hardness of the modules, as well as increase the granularity by moving from $2 \times 2 \text{ cm}^2$ cells to $1.5 \times 1.5 \text{ cm}^2$ cells of the SpaCal WGAGG modules. A basic schematic of a SpaCal module with continuous fibers is shown in figure 3.4.

3.2. Assembly of a new SpaCal WPoly prototype

Table 3.1: SpaCal module types to be installed in LHCb during LS3 and LS4 [22].

absorber	tungsten (W)		lead (Pb)
installation	LS3	LS4	LS3/LS4
fibers	polystyrene	GAGG	polystyrene
cell size	$2 \times 2 \text{ cm}^2$	$1.5 \times 1.5 \text{ cm}^2$	$3 \times 3 \text{ cm}^2$
Moliere radius	1.8 cm	1.46 cm	$\sim 3 \text{ cm}$
radiation length	0.72 cm	0.62 cm	$\sim 1 \text{ cm}$
longitudinal sections	19 cm	(4.5 + 10.5) cm	29 cm/(8 + 21) cm

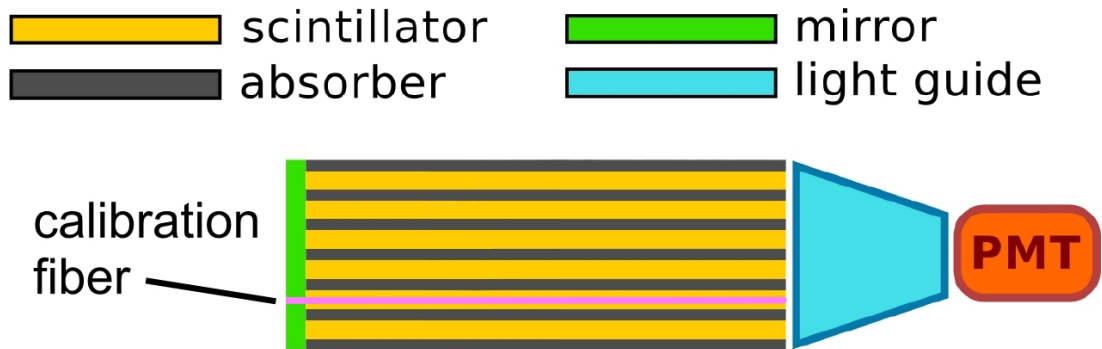


Figure 3.3: A schematic of a SpaCal module without longitudinal segmentation.

3.2 Assembly of a new SpaCal WPoly prototype

In February 2023, four pieces of 3D-printed tungsten absorber were produced by a German company EOS [23], and delivered to CERN. Through collaborative R&D efforts, and after testing a few smaller samples, a successful attempt was made to produce four absorber pieces of $121 \times 121 \text{ mm}^2$, matching the size of the SpaCal tungsten calorimeter module. Three of the four received pieces were 5 cm long, and one was 4 cm long. Putting the four together gives 19 cm, corresponding to $25 X_0$ of the SpaCal WPoly modules. The surface quality was good with a mean roughness of $R_a = 5 \mu\text{m}$, an average profile height deviation from the mean. It was possible to insert the fibers inside the absorber holes, where their nominal sizes are 1.0 and 1.2 mm, respectively, without visible damage to fibers when pushing them inside.

After the initial tests, the prototype assembly continued in the following steps:

- development and production of a support structure
- fiber cutting, fiber insertion, fiber gluing, fiber polishing
- development and installation of a calibration system
- development and production of hollow light guides

- development and production of PMT holders
- characterization of PMT voltage divider boards
- PMT installation

Many of these steps could be done in parallel. In total, the assembly took five weeks and was finished on time before a first test beam at DESY in May 2023.

3.2.1 Development and production of the support structure

To align the four absorber pieces a support structure shown in figure 3.4 was used. The absorber pieces were enclosed with four aluminum walls held together by screws. It was ensured that the wall pieces were always mounted in the same positions to maintain consistent mechanical stability. Additionally, the aluminum walls provide a way to attach other components to the prototype, such as handles, a glue bath, a light guide, a mirror, a bottom plate, etc. In the calorimeter, such an approach will not be possible because it would introduce too much dead space between the modules, but for the current prototype, this was the most practical solution.

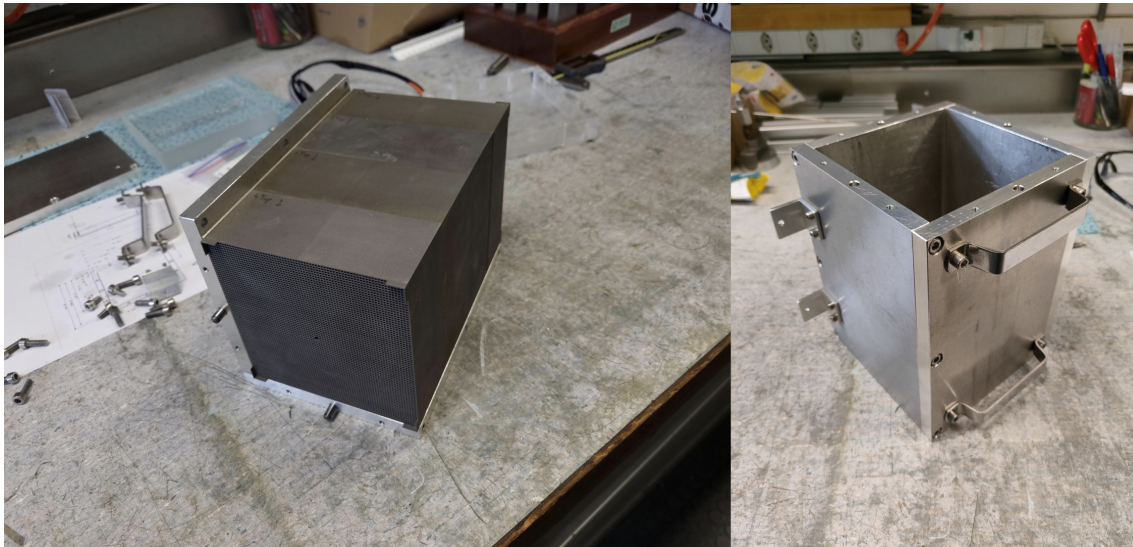


Figure 3.4: (a) Four aligned absorber pieces. (b) Aluminum walls forming a box.

3.2.2 Fiber cutting

The SpaCal WPoly module-size prototype uses SCSF-78 plastic scintillating fibers produced by Kuraray [17]. They are square in cross-section with a size of $1 \times 1 \text{ mm}^2$, matching the shape of the holes in the absorber. The emission peak of the scintillation light is 420 nm, and the scintillation decay time is 2.7 ns. The fibers were delivered on a spool as a single 1300 m long thread. Therefore, the fibers had to be cut into 22 cm long pieces before insertion into the absorber. It was important to keep the cutting length tolerance as low as possible. For this reason, a simple cutting method was developed. The fiber thread was guided from the spool into a 22 cm long aluminum straw fixed to a table. It was pushed inside this straw until it reached the end and then was cut on the other side. The cut fibers were afterward placed inside plastic bags, as seen in figure 3.5, to protect them from dust.



Figure 3.5: (a) The author cutting fibers. (b) Cut fibers inside a plastic bag.

3.2.3 Fiber insertion

The absorber can be divided into 36 cells arranged in a 6×6 grid. Each cell consists of 12×12 holes that host the scintillating fibers. In total, the prototype holds 5184 scintillating fibers. The fiber insertion was done by hand because the orientation of the fibers was important. Since the fiber thread was stored for a long time on a spool, the cut pieces of 22 cm were slightly bent. If no attention had been paid to the orientation of the inserted fibers, the ones placed on the edges of a cell could bend outwards into a neighboring cell. This would introduce inhomogeneities in the response and had to be avoided. Therefore, the fibers were inserted such that all of them bend towards the cell center, as shown in figure 3.6. The whole fiber insertion process took place in a dedicated "clean room" to avoid dust collection, and stacks of fibers were additionally cleaned with an ionized air gun to remove the remaining traces of dust before they were used for insertion. Gloves were also used during the insertion to prevent sweat and body oils from contaminating the fiber surface, which could damage the fiber cladding over time.

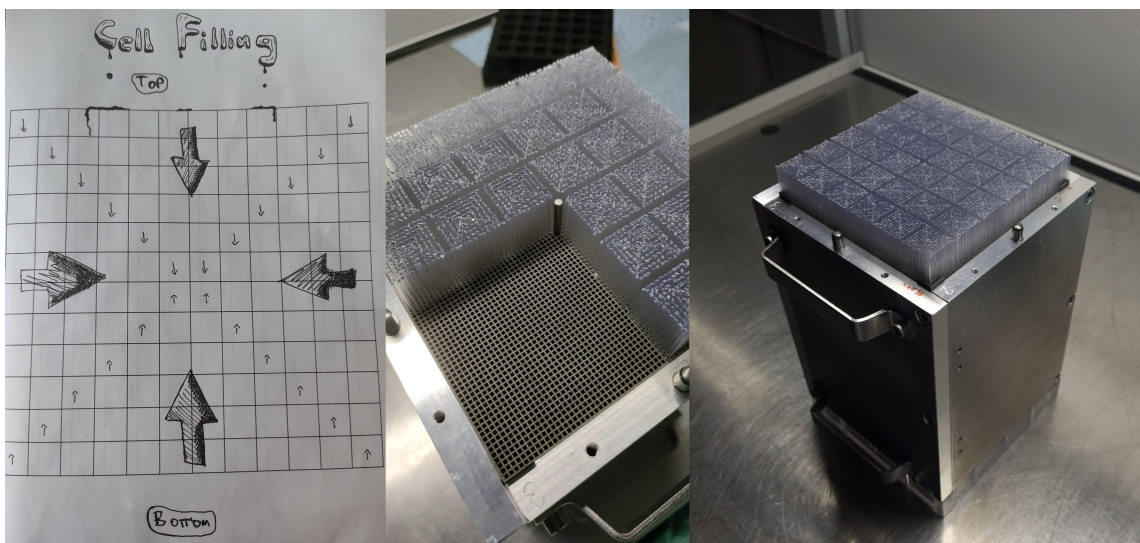


Figure 3.6: (a) Schematic showing the bending orientation of fibers during insertion. (b) Absorber with 3/4 of total fibers inserted. (c) Absorber filled with all 5184 fibers.

3.2.4 Fiber gluing

After the insertion, the fibers had to be glued together. This allowed us to polish them all together and further reduce their length differences, which could otherwise introduce inhomogeneities in the response of the prototype. For the glue, we used Araldite 2011 [24], a common choice in detector construction at CERN. Its properties and aging behavior are well studied, and it is transparent to light and non-corrosive to plastic. The fibers stick about 1 cm out of the absorber but they have to be glued in such a way that the glue does not reach the absorber pieces. This is needed because in the future the polystyrene fibers will be replaced by GAGG crystal fibers to study the properties of a SpaCal WGAGG module. The gluing process proceeded in three steps. First, a calculated amount of glue was purred inside a "glue bath" made out of plexiglass. Next, the absorber holding the fibers was lowered into the glue bath so that only the tips of the fibers, sticking out of the absorber, entered the glue. The last step was putting the absorber, together with the glue bath, inside an oven heated to 50 °C, as seen in figure 3.7, to let the glue harden. It was left there overnight, and the next morning, the same steps were repeated for the other side.

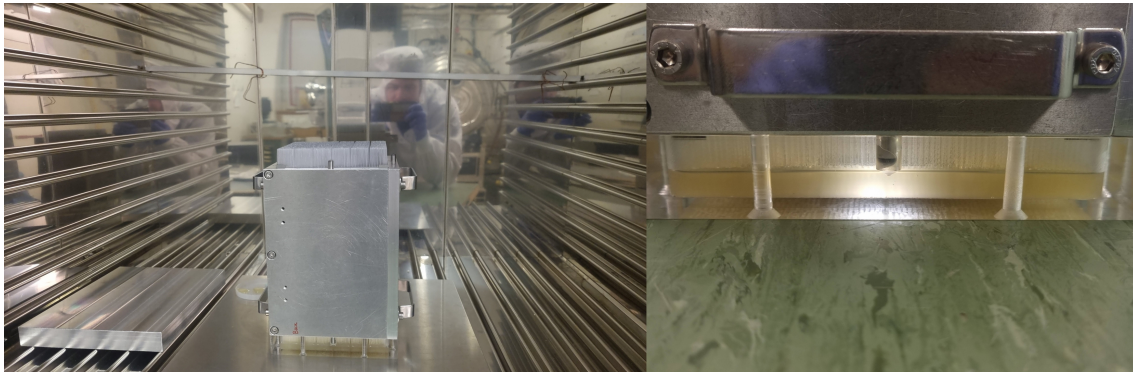


Figure 3.7: (a) Absorber placed inside an oven. (b) The glue level after hardening.

3.2.5 Fiber polishing

To polish the fibers, we used a specialized machine, shown in figure 3.8, paired with a diamond milling cutter. The method achieved the desired precisions without leaving unwanted patterns on the polished surface or breaking any of the fibers.

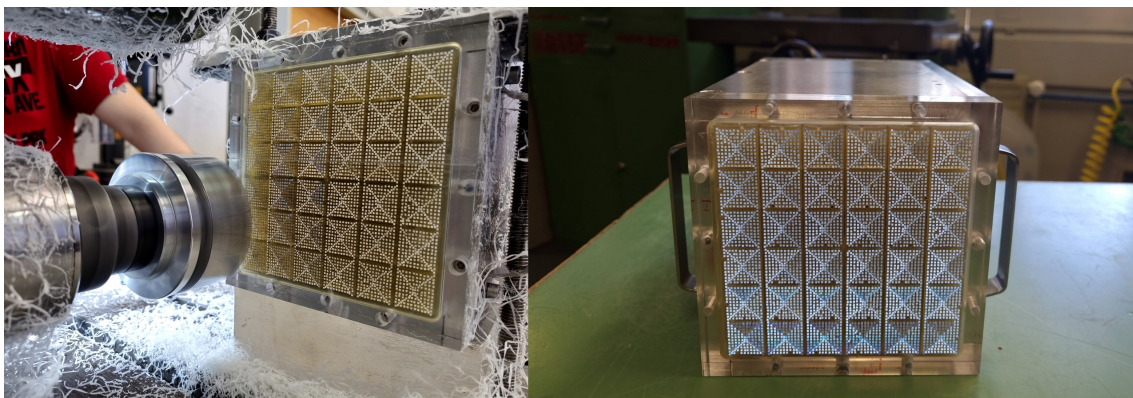


Figure 3.8: (a) Prototype during fiber polishing. (b) Prototype after fiber polishing.

3.2.6 Development and installation of calibration system

An LED-based calibration system is an important part of the prototype. It allows to monitor the response of the PMTs over time and adjust their gain when needed. From each cell, one scintillating fiber was drilled out and replaced with a clear fiber of similar length. One end of each clear fiber was then glued inside a (gray) plastic holder, as seen in figure 3.9, which keeps it in place. The plastic holders serve as connectors to which external clear fibers coupled to a single LED are connected.



Figure 3.9: (a) Gluing the inserted optical fibers inside plastic holders. (b) External set of optical fibers connected to the front side of the prototype. (c) Red LED light seen through the hollow light guide on the back side of the prototype.

3.2.7 Development and production of hollow light guides

The module-size SpaCal WPoly module was equipped with 16 Hamamatsu R14755U-100 photomultiplier tubes [25]. The photocathode area of this PMT does not match the area of a cell. Therefore, a light guide is needed to collect the light from a larger area and focus it on a smaller one. The light collection efficiency of a light guide can never be 100%, and it decreases with the increasing ratio between the entrance and exit area. In this case, the scintillation light from a square area of $20 \times 20 \text{ mm}^2$ had to be guided to a circle with a diameter of 8 mm. The light guides were made hollow by design for several reasons. From irradiation studies on PMMA-based light guides, it is known that their light efficiency decreases over time due to radiation-induced effects, such as a decrease in the light absorption length. Secondly, the price of the hollow light guides is much lower compared to that of PMMA ones, and they could be produced in the laboratory at CERN. They are based on a 3D-printed plastic holder, shown in figure 3.10, inside which a reflective ESR foil is glued. The ESR foil was cut to the desired dimensions with a laser cutter, and then the shapes were pre-folded and inserted inside the plastic holder. The exiting side of the light guide includes a "clicking mechanism" which aligns and holds the PMTs in place.

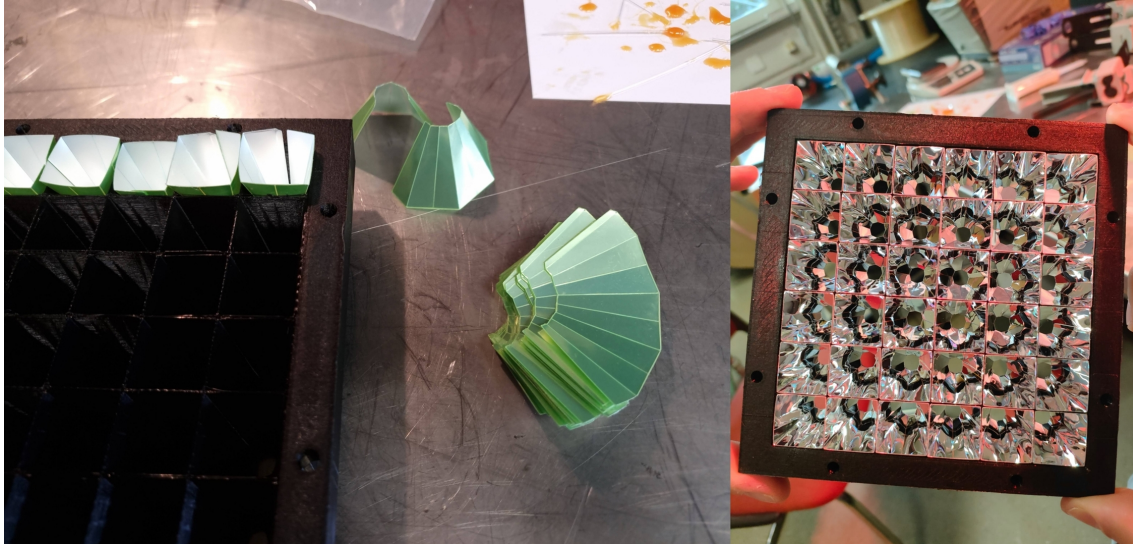


Figure 3.10: (a) Insertion of the reflective ESR foil shapes inside the plastic holder. (b) Finished hollow light guide seen from the front side.

3.2.8 Development and production of PMT holders

The first part of the PMT holder is already integrated into the exiting side of the hollow light guides. However, due to the weight of the PMT voltage divider boards and the cables, the PMTs would bend out of position over time. To offer more stability, a plexiglass plate was designed, shown in figure 3.11, which sits on the outer edge of the PMTs and pushes them securely inside the hollow light guide.



Figure 3.11: (a) "Clicking mechanism" of the hollow light guide. (b) An additional plexiglass plate mounted on the back side of the prototype with a set of screws.

3.2.9 Characterization of PMT voltage divider boards

PMT voltage divider boards are used to distribute a single input high-voltage (HV) between each of the dynodes inside the PMT structure. The voltage repartition

3.2. Assembly of a new SpaCal WPoly prototype

ratios were set equal for all dynodes. The divider boards, shown in figure 3.12, were produced at ICCUB Barcelona [26] and tested before the final prototype assembly.

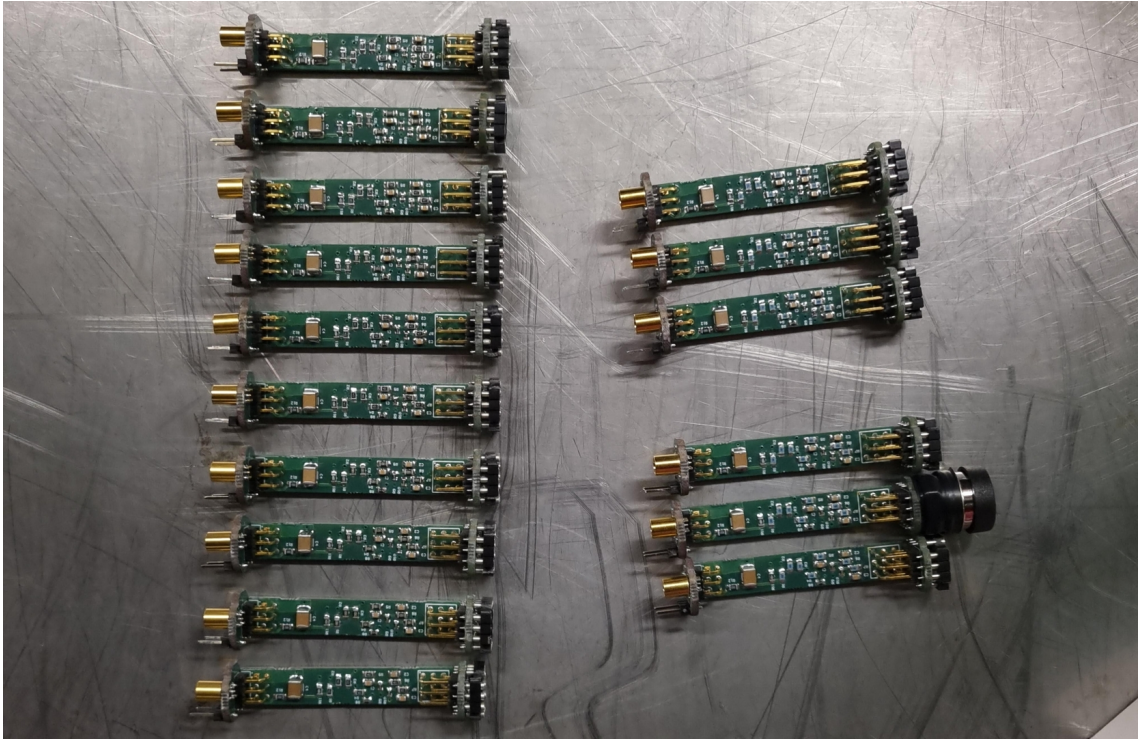


Figure 3.12: A set of 16 voltage divider boards. A PMT is attached to one of them.

3.2.10 PMT installation

The PMT voltage divider boards have a two-pin connector to supply the HV and an MCX connector to read the signal. After the first installation, "board - PMT" pairs, shown in figure 3.13, were made, and at the next installation, the same PMT could be paired with the same board and used for the same cell of the prototype.

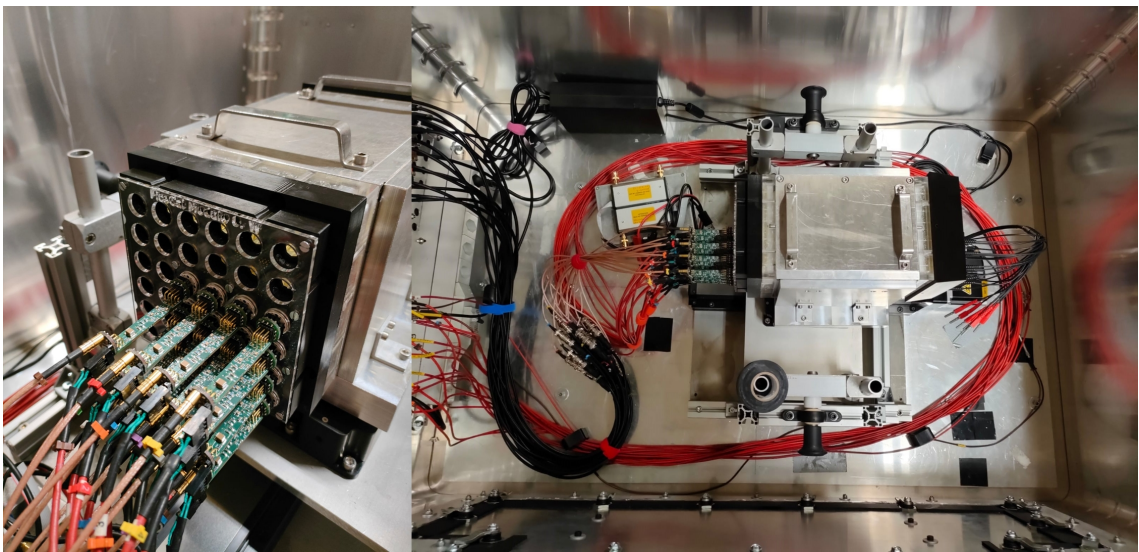


Figure 3.13: (a) Back side of the prototype. (b) Prototype inside the test beam box.

3.3 Photodetector characterization

The choice of a photodetector for a physics experiment is not a trivial task. It often requires years of R&D, multiple characterization studies, and collaboration between numerous institutions and companies. A candidate photodetector for the SpaCal region of the LHCb ECAL has to satisfy the following requirements [22]:

- Fits inside a 15×15 mm² square, matching the cell size of SpaCal WGAGG.
- Radiation hard. Has to withstand up to 1 MGy in the innermost region.
- Response non-linearity below 1% in the relevant energy range.
- Fast time response with O(10ps) time resolution.

From a wide selection of photodetectors, photomultiplier tubes stand out as the best candidate. They can be made compact, are radiation tolerant, and can have a fast time response. In addition, these detectors have been used in calorimetry for many decades, so their general properties and shortcomings are relatively well understood.

3.3.1 Response non-linearity measurements

A few methods to measure the response non-linearity of different PMT models were explored before the following method, reported in [15], was chosen as the best approach. In this method, we use a pair of LEDs (instead of one), each connected to one channel of an LED driver. The LED pair sits on a digitally controllable linear translation stage, with which we change their distance to the PMT. The PMT is fixed to an optical bench, and the whole setup is enclosed inside a dark box. In this measurement, one LED provides a low-intensity pulse and the other a high-intensity pulse. The two pulses alternate with a frequency determined by a pulse generator. The high and low-intensity pulses are fixed to a ratio of around 4:1. At low light levels, where the PMT is assumed to be linear, the ratio between the response to the high-intensity LED pulse (I_{H0}) and the response to the low-intensity LED pulse (I_{L0}) should be equal to 4. When the LED light source is moved closer to the PMT, and the subsequent light intensity increases, the PMT's response starts to deviate from linearity. If I_L and I_H are PMT responses at higher light levels to low-intensity and high-intensity pulses, respectively, then non-linearity can be calculated as [15]:

$$\text{non-linearity} = \frac{(I_H/I_L) - (I_{H0}/I_{L0})}{(I_{H0}/I_{L0})} \times 100\% \quad (3.1)$$

Non-linearity is usually expressed as a percentage and represents the deviation from the ideal line of response. As an example, if a PMT in a certain configuration gives a 200 mV signal pulse at beam energy of 20 GeV, with 10% non-linearity, it will only respond with a 900 mV pulse at 100 GeV, which is 100 mV less than expected.

Figures 3.14 and 3.15 show the linearity measurement setup. A diffusor placed in front of the LEDs ensures a more homogeneous light distribution. Operation of the LEDs is more stable when they work at higher voltages, corresponding to higher intensities. Therefore, in configurations where the PMT has a high gain, additional optical attenuation is used to decrease the amount of light incident on the PMT.

The PMT signal first goes into an attenuator with adjustable attenuation values. This is needed to match the PMT's pulse heights to the dynamic range of the DRS4-based [27] digitizer. It accepts signal heights from -500 mV to 500 mV, and it records the signal waveforms inside a time window of 200 ns at a sampling speed of 5 GS/s. The digitizer is connected to a computer that stores the signal waveforms.

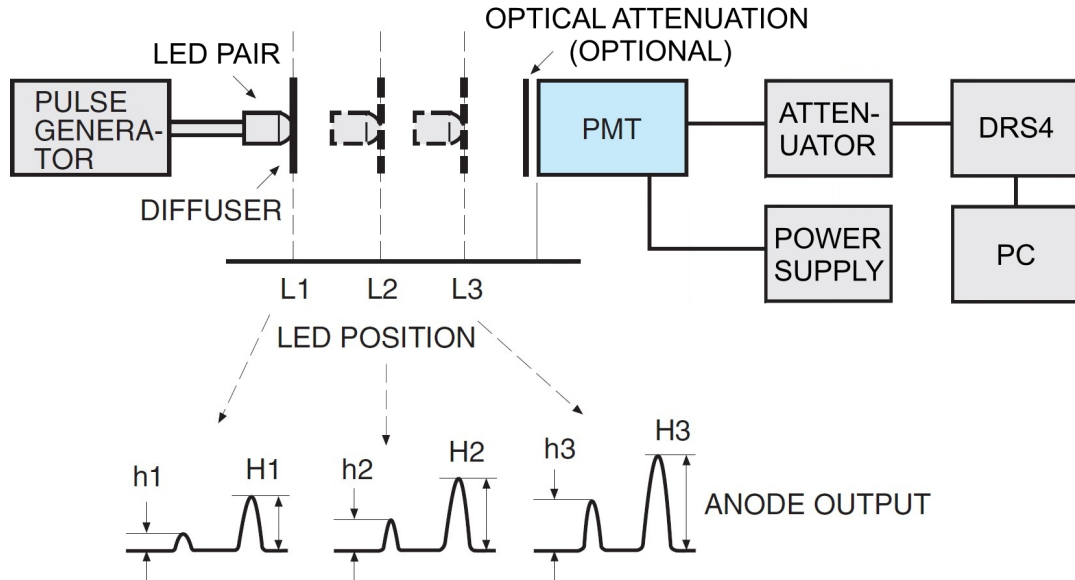


Figure 3.14: Diagram of the response non-linearity measurement setup.

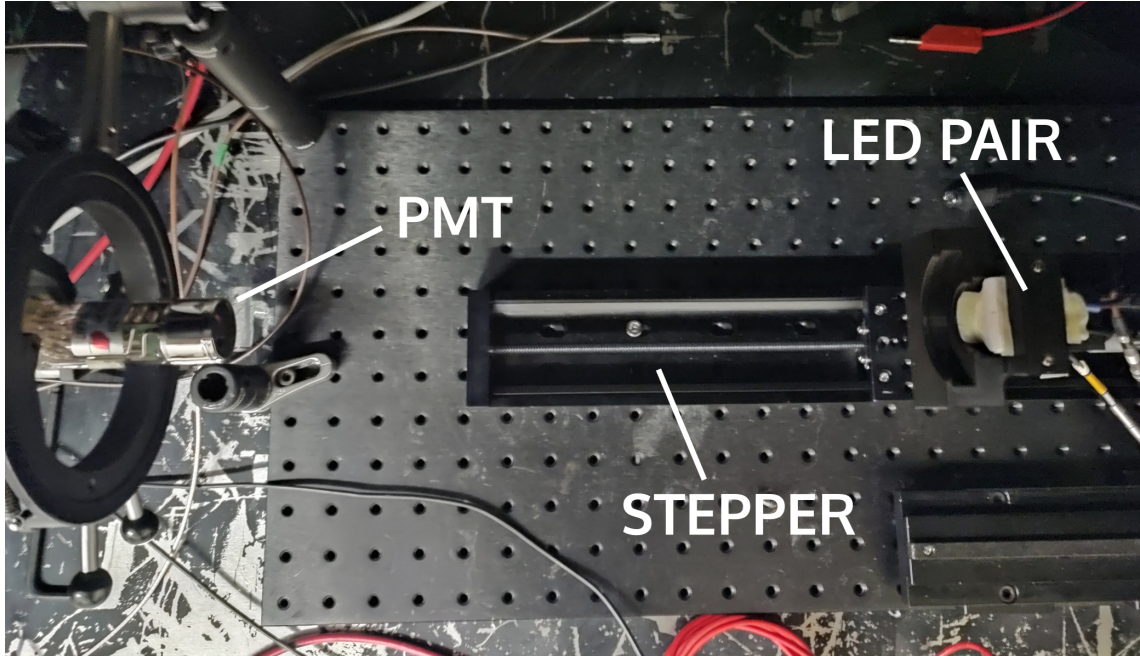


Figure 3.15: Response non-linearity measurement setup.

Figures 3.16 and 3.17 show an example measurement with the Hamamatsu R7899-20 PMT [28], the standard ECAL PMT currently used in the Shashlik modules. This PMT is suitable for testing the linearity measurement setup because its linearity properties were well-studied with different methods in the past. Figure 3.16

shows the measured response ratio between the high-intensity and low-intensity LED pulses. From this plot, using equation 3.1, where the red point is the reference (expected) response ratio, the non-linearity, shown in figure 3.17, is obtained. At present, the setup allows measuring the non-linearity with 1-2% precision. This level of precision is due to non-linearity effects present in the setup, such as time-dependent fluctuations of the LEDs shown in figures 3.18 and 3.19. Additional contributions to the uncertainty come from the electronic noise of the digitizer and the misalignment of the LED pair with respect to the PMT center.

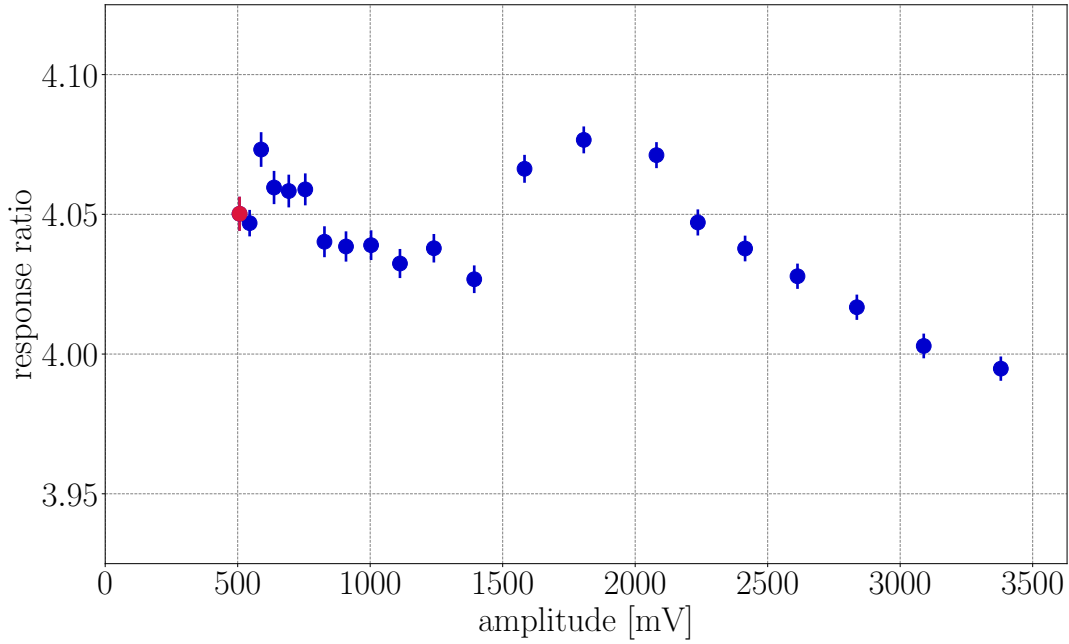


Figure 3.16: Response ratio with respect to the response to high-intensity LED.

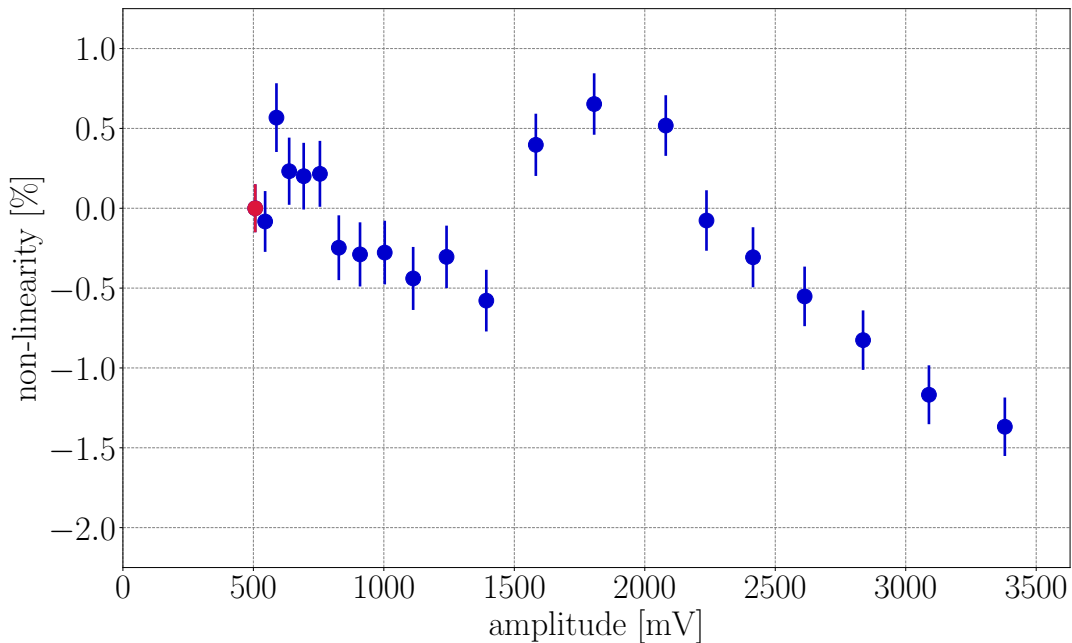


Figure 3.17: Non-linearity with respect to the response to high-intensity LED.

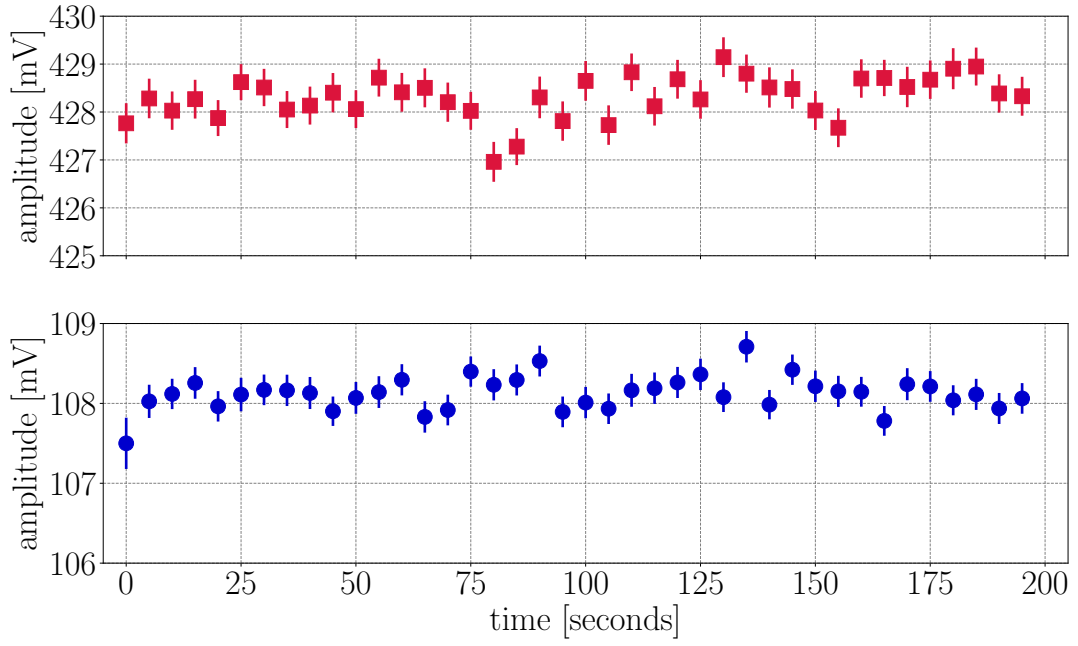


Figure 3.18: Time-dependant fluctuations of led 1 (top) and led 2 (bottom).

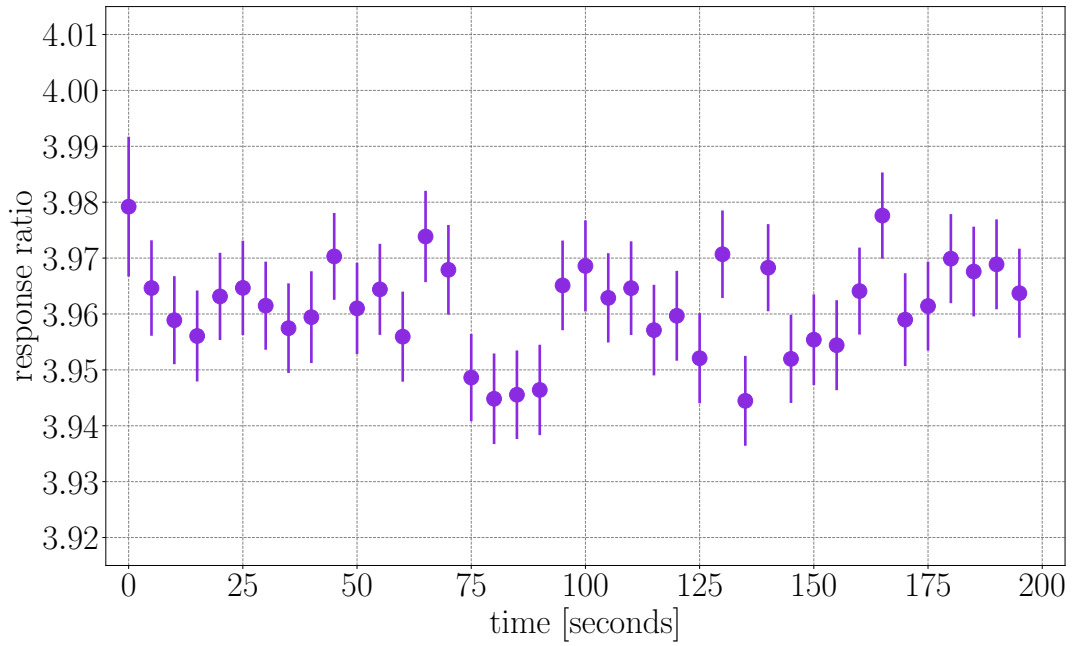


Figure 3.19: Time-dependant fluctuation of the response ratio at a fixed position.

4. Test beam results

Test beam campaigns are essential in any development of detectors intended for high energy physics experiments. Research facilities like CERN or DESY, which house large accelerators, such as the Super Proton Synchrotron (SPS), provide access to beams of different particle types with a well-defined energy, commonly known as "test beams". These campaigns aim to study detector behavior under conditions that closely resemble those encountered in high energy physics experiments.

4.1 Test beam setup

While minor modifications to the test beam setup were made over time, the general layout remained consistent as described in [20] and is shown in figure 4.1.

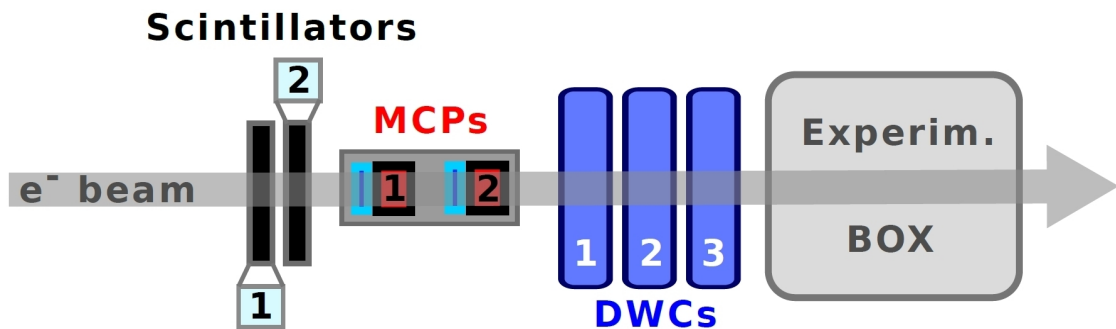


Figure 4.1: The electron beam moves from left to right, two scintillating pads provide the trigger signal, two MCPs the time reference, and three DWCs the tracking information. The experimental box contains the prototype and the rotating steppers.

The main elements of the test beam setup, also shown in figures 4.2 and 4.3, are:

1. Two scintillating pads operated in coincidence provide a trigger signal to the data acquisition system that opens a common gate and distributes it to the other detector elements. This synchronization starts the data writing to the storage and provides a way to align all detector elements in time.
2. Microchannel plate photomultiplier tubes (MCP-PMTs, or shorter MCPs) serve as a time reference due to their inherent good time resolution when paired with a Cherenkov radiator. Utilizing two MCPs in sequence allows for monitoring the time resolution of the time reference on a run-to-run basis. As a bonus, it further improves its timing precision by a factor of $\sqrt{2}$ when using the average time stamp from both as the time reference. This test beam setup achieves a reference time resolution of 15-20 ps. Since the MCP pair is the smallest element in the chain, it also defines the usable size of the beam.

3. Delay wire chambers (DWCs) are a type of gaseous tracking detector. Utilizing a set of three chambers not only enhances the measurement of the particle's hit positions but also enables the measurement of its incidence angle.
4. To prevent any ambient light from reaching the photodetectors instrumented in the prototype, the prototype under test is enclosed within a light-tight box. The prototype sits on a set of externally controlled rotating steppers, allowing it to change its orientation with respect to the beam.

Two options for the signal readout electronics are used non simultaneously, as a part of two different setups, for the results shown in the following [20]:

1. For the energy resolution measurements, the signals are integrated over a 400 ns gate using 3 LeCroy 1182 ADC modules.
2. For the time resolution measurements, the waveforms are digitized using the DRS4-based [27] V1742 CAEN digitizer with 5 GS/s and 500 MHz bandwidth.

The signal data is then saved to a computer placed inside the test beam area and later copied to a computer inside the control room for online and offline analysis.



Figure 4.2: The test beam setup in June 2023 at SPS.

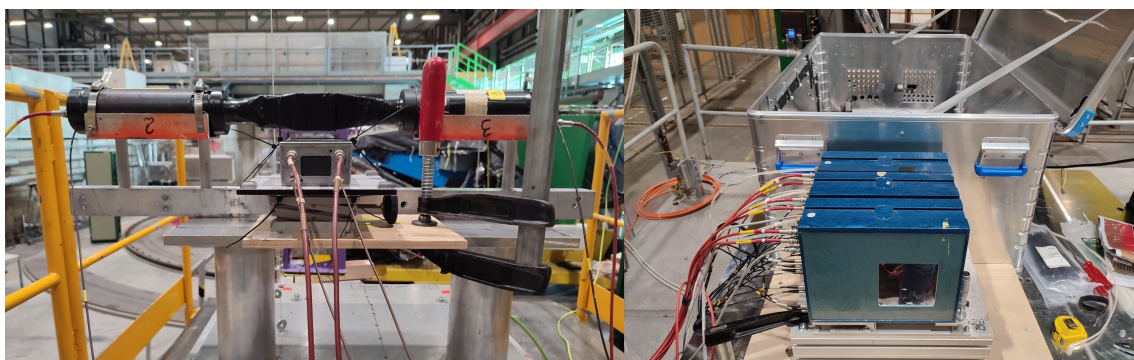


Figure 4.3: (a) Scintillator pads and MCPs. (b) DWCs and prototype box.

4.2 Time resolution

One of the promising enhancements to the electromagnetic calorimeter of the LHCb experiment during LS4 includes the addition of capabilities for a precise particle time-of-arrival measurement. The time resolution of a scintillator-based calorimeter depends on the combined performance of its underlying elements. It is determined by various factors, including but not limited to the characteristics of:

1. Scintillators, in particular by their scintillation rise and decay times.
2. Photodetectors, for example, by their transit time spread (T.T.S.), which is the transit time fluctuation of photoelectron pulses when the photocathode is fully illuminated with single photons [15].
3. Readout electronics, where the noise contribution can deteriorate the timing measurement for pulses with a lower signal-to-noise-ratio.

A standard approach to measure the time resolution of a detector is by fitting the distribution $t_{\text{ref}} - t$ with a Gaussian function, where t_{ref} and t are reference time and measured time by the detector. The time resolution is given as the sigma of the fitted Gaussian function after subtracting the reference contribution in quadrature.

Due to time constraints during test beam campaigns, the timing characteristics and performance are evaluated for the central four cells of the 4×4 cell matrix. For prototyping purposes and because of cost limitations, we only instrumented a matrix of 4×4 cells with PMTs, as shown in figure 4.4, instead of all 36 cells. Such a setup was sufficient for both time resolution studies as well as energy resolution studies. The prototype includes a screw hole in the middle, which sits in between cells 1, 2, 5, and 6. It was initially designed as a solution to provide mechanical stability to the modules when installed in the experiment, without the use of the metal support structure, and to study its impact on performance during the prototyping phase.

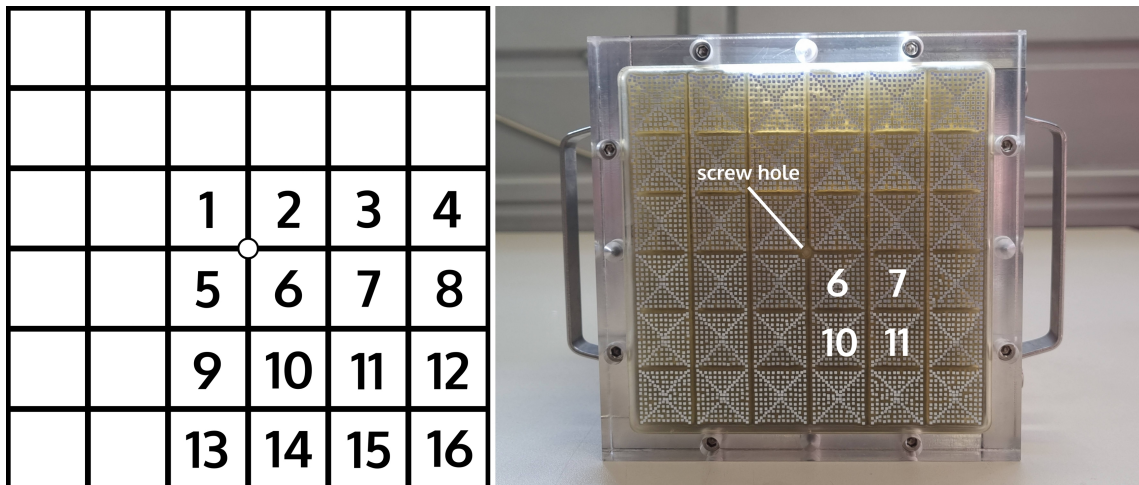


Figure 4.4: (a) Labeled schematics of the instrumented cell matrix. (b) Screw hole and the four cells in the center of the cell matrix used for timing measurements.

4.2.1 Scan for optimal voltage

The high voltage applied to a PMT is an important parameter of the device as it influences its response characteristics. This also concerns timing measurement and the optimal voltage at which the time resolution is the lowest is selected empirically after a scan over a subset of allowed high voltage values.

Measurements and results - DESY

At DESY, the available electron beam energies with a sufficient rate, range from 1 to 5 GeV. The amount of scintillation light an electron at this energy produces after it creates an electromagnetic shower inside the prototype is relatively low and hard to detect with Hamamatsu R14755U-100 PMTs that have a maximum gain of $\sim 6 \times 10^4$ at a high voltage of 1000 V. Therefore, a set of amplifiers was used to amplify the signal by a factor of ~ 13 before feeding it into the digitizer.

The constant fraction discrimination (CFD) method, further discussed in chapter 4.2.2, samples the signal at a percentage of its peak amplitude to obtain the timestamp. Figure 4.5 shows the results of the voltage scan. It was performed at 5 GeV, and a CFD threshold of 0.2 was used in the analysis. As optimal voltages, we chose 700 V for cells 6 and 7, 600 V for cell 10, and 650 V for cell 11. These values were then used for the subsequent measurements.

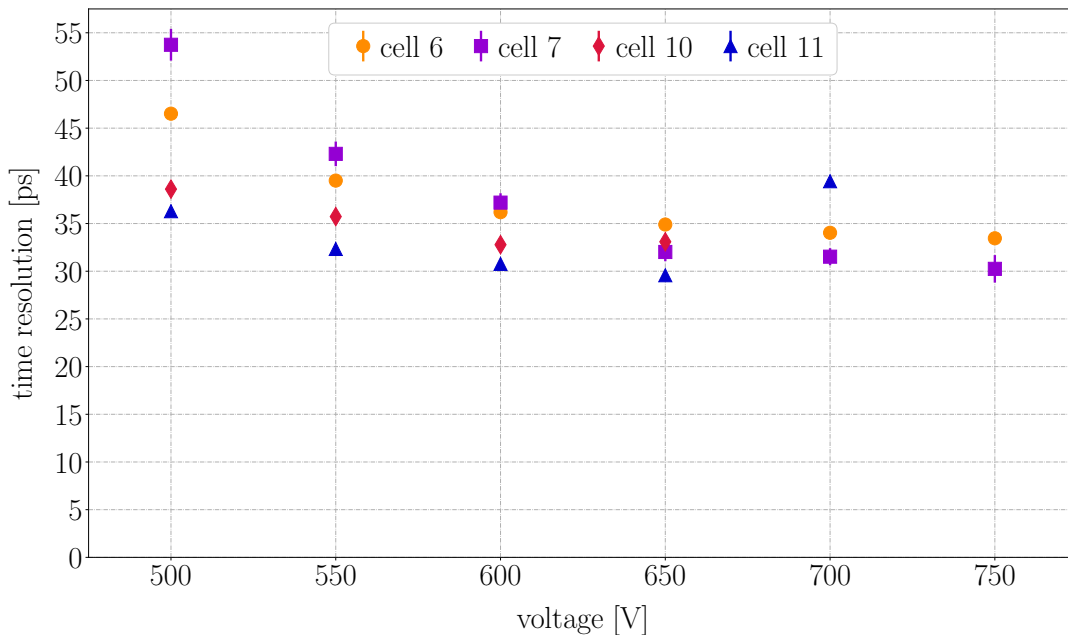


Figure 4.5: Scan for optimal voltage at DESY.

Measurements and results - SPS

Similarly, we had to perform a voltage scan at SPS to find the optimal working voltages for each of the four cells for which we measured their time resolution. At SPS, we performed measurements with electron beam energies from 20 to 100 GeV, and at these energies, the amount of scintillation light produced is high, and no additional signal amplification is needed. In fact, the signal is high enough that at some voltages, we saturate the digitizer and have to attenuate the signal. For

this purpose, we used a set of externally controllable attenuators with adjustable attenuation steps and wide frequency bandwidth. We performed the voltage scan at 100 GeV and used a CFD threshold of 0.75 in the analysis. As seen from figure 4.6, the optimal voltages are 500 V for cells 6 and 10, 550 V for cell 7, and 450 V for cell 11. Due to time constraints and difficulties with the beam, the voltage scan was extended to lower voltage values only for cell 11.

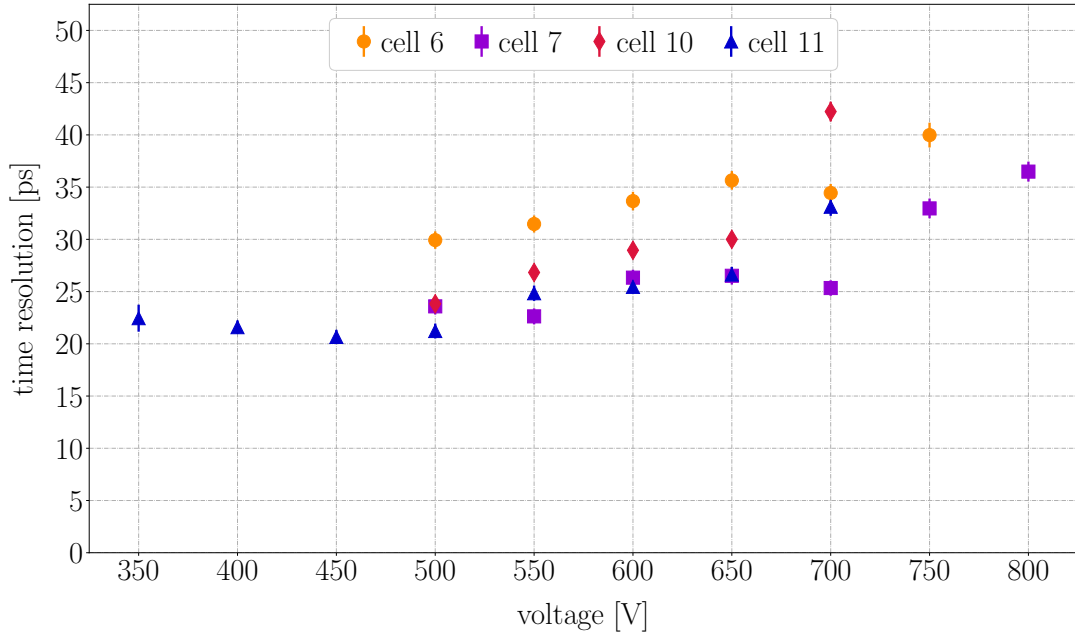


Figure 4.6: Scan for optimal voltage at SPS.

4.2.2 Scan for optimal CFD threshold

A common approach for measuring time of arrival is to look for the intersection of the signal with the time axis at the moment when the signal crosses a fixed voltage threshold. However, this method is susceptible to the variation of pulse height, and a so-called *time walk* effect is observed. The constant fraction discrimination (CFD) method addresses this issue by using a variable threshold set to a fraction of the pulse height. This technique provides amplitude-independent information on the event time and is suitable for use in calorimetry in high energy physics.

It turns out that the choice of the CFD threshold is not always trivial. The time resolution can be improved in some cases by sampling the signal closer to its baseline, and other times, closer to its peak. The optimal CFD threshold, one that gives the best time resolution, can be empirically determined by performing a scan over possible values. This is usually done each time a change to the detector setup is made, such as swapping the PMT with another type of PMT or going from a single-sided readout to a double-sided readout configuration.

Measurements and results - DESY

At DESY, the CFD threshold scan was performed at 5 GeV and optimal PMT voltages. The obtained curve shown in figure 4.7 is relatively flat with a minimum at around 0.2 which was selected as the optimal CFD threshold.

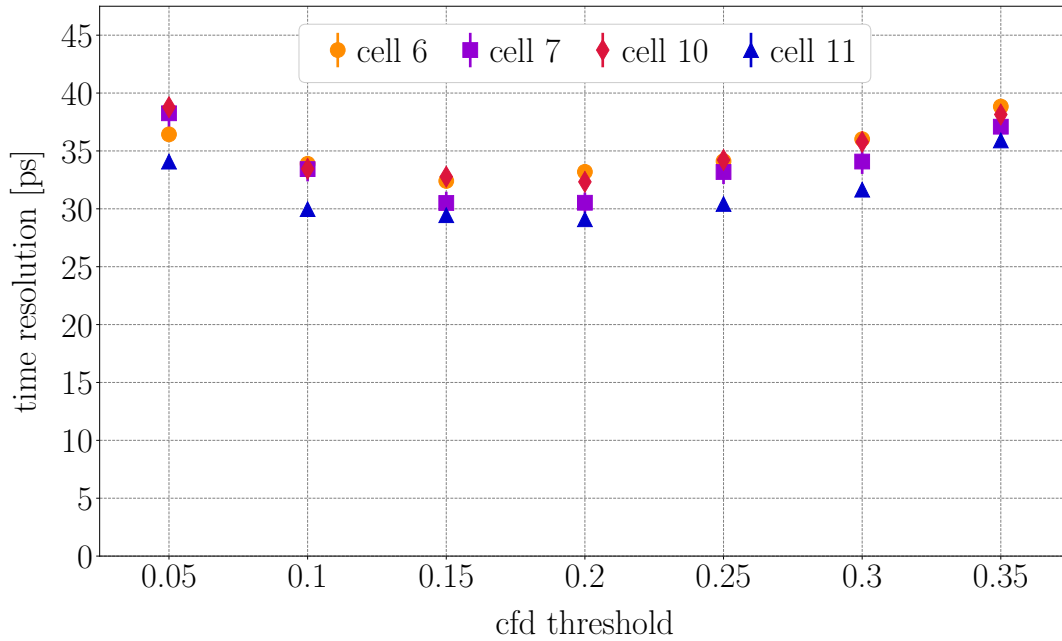


Figure 4.7: Scan for optimal CFD threshold at DESY.

Measurements and results - SPS

At SPS, the CFD threshold scan was performed at 80 GeV. Due to a mistake, non-optimal voltages for cells 6, 7, and 10 of 740 V, 760 V, and 660 V, respectively, were used. For cell 11, 500 V was used, which had a similar timing performance as 450 V but a higher signal at 20 GeV, and hence a better timing performance at lower energies. The results of the CFD scan are shown in figure 4.8.

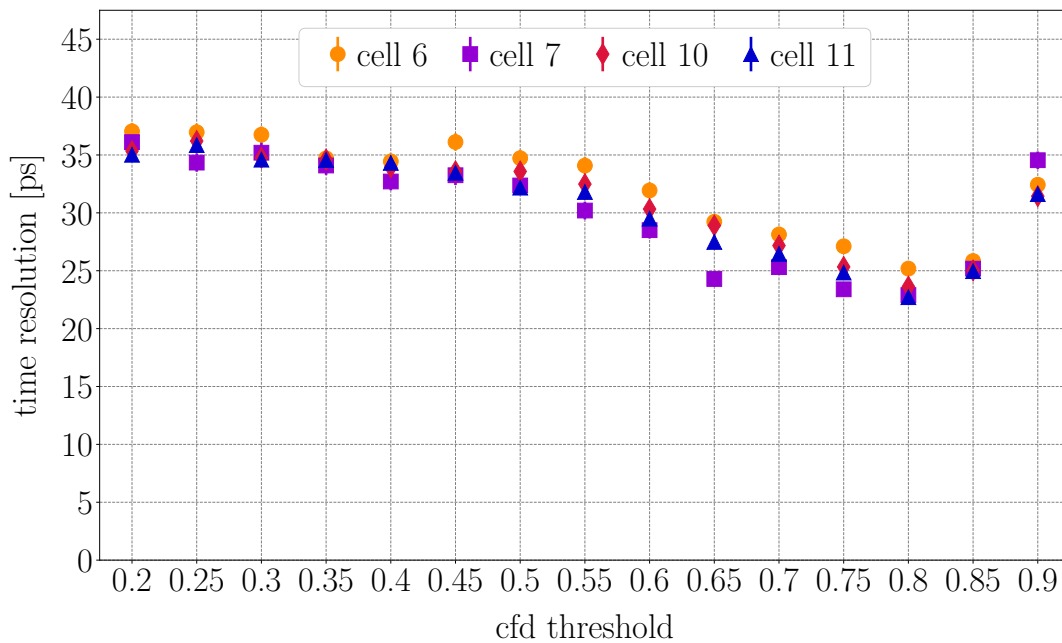


Figure 4.8: Scan for optimal CFD threshold at SPS.

Compared to DESY, the optimal CFD threshold is moved to higher values at SPS and has a minimum of around 0.75, which was selected as the optimal value. It is worth noting that these results agree with the results from previous test beams.

4.2.3 Time resolution with respect to beam energy

The time resolution depends on the energy because the signal amplitude and shape change with energy. Fluctuations in the signal shape will introduce fluctuations in the timing measurement and have an impact on the time resolution. Additionally, the number of photons produced in a shower and detected by the PMT increases with the beam energy, which improves the timing measurement. However, this effect saturates once the photodetector sees enough light, and the time resolution becomes dominated by constant contributions.

Measurements and results - DESY

At DESY, the time resolution of the four cells was measured at five different energies, as shown in figure 4.9. Cell 11 performed the best at all energies. Its time resolution at 5 GeV is around 30 ps. One possible explanation is that cell 11 is the one that is the furthest away (out of the four) from the screw hole in the middle of the module, and hence has the largest shower containment and the smallest signal fluctuations.

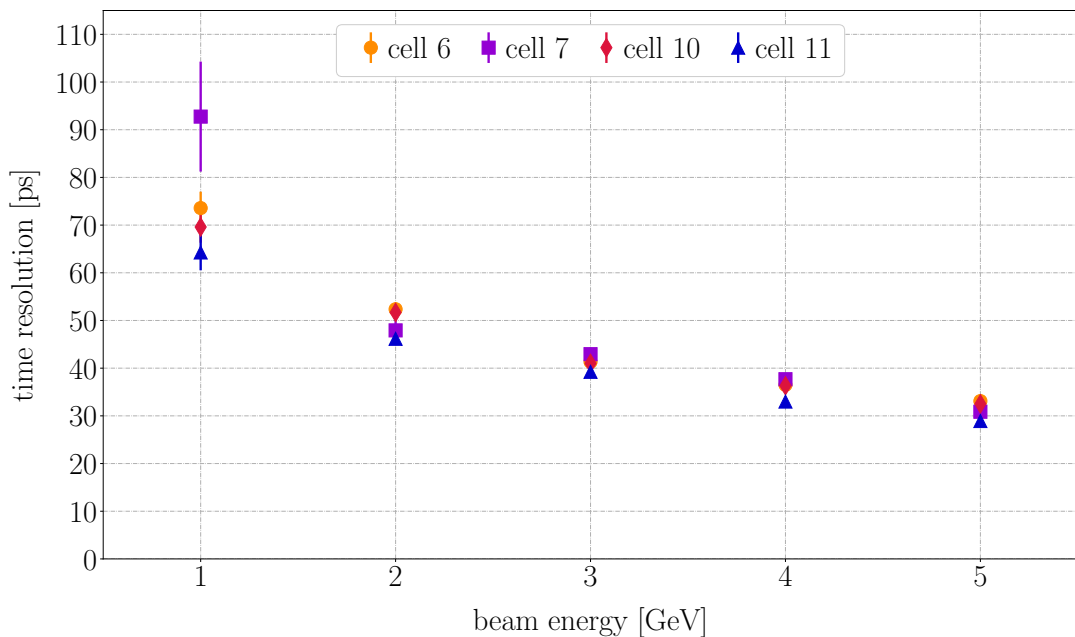


Figure 4.9: Time resolution with respect to beam energy at DESY.

Measurements and results - SPS

At SPS due to time constraints, we could only measure the timing performance at five different energies for one of the four previously studied cells. We chose cell 11 because it was the best-performing one at DESY and the same was observed at SPS from the voltage scans and CFD threshold scans. Nevertheless, the time resolution curve flattens at around 60 GeV, as seen in figure 4.10, where it approaches 20 ps. This indicates that the amount of scintillation light is sufficiently high at such energies, and constant contributions begin to dominate the time resolution.

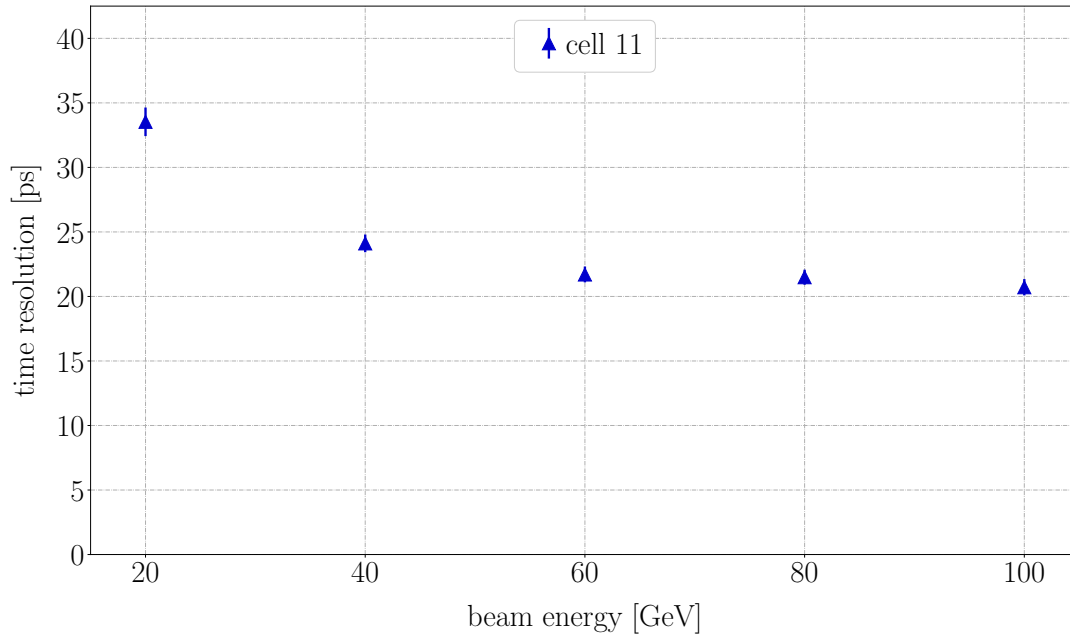


Figure 4.10: Time resolution with respect to beam energy at SPS.

Comparison of timing performance at DESY and SPS

The SpaCal region of the future LHCb ECAL has to demonstrate sufficient performance in the energy range from a few to a few hundred GeV. After LS4, this includes the timing performance, which can be studied by combining the test beam results from DESY and SPS campaigns. Figure 4.11 shows DESY and SPS data for cell 11. There is a step between 5 and 20 GeV that can be understood due to the different data-taking conditions, for example, the use of amplifiers and attenuators.

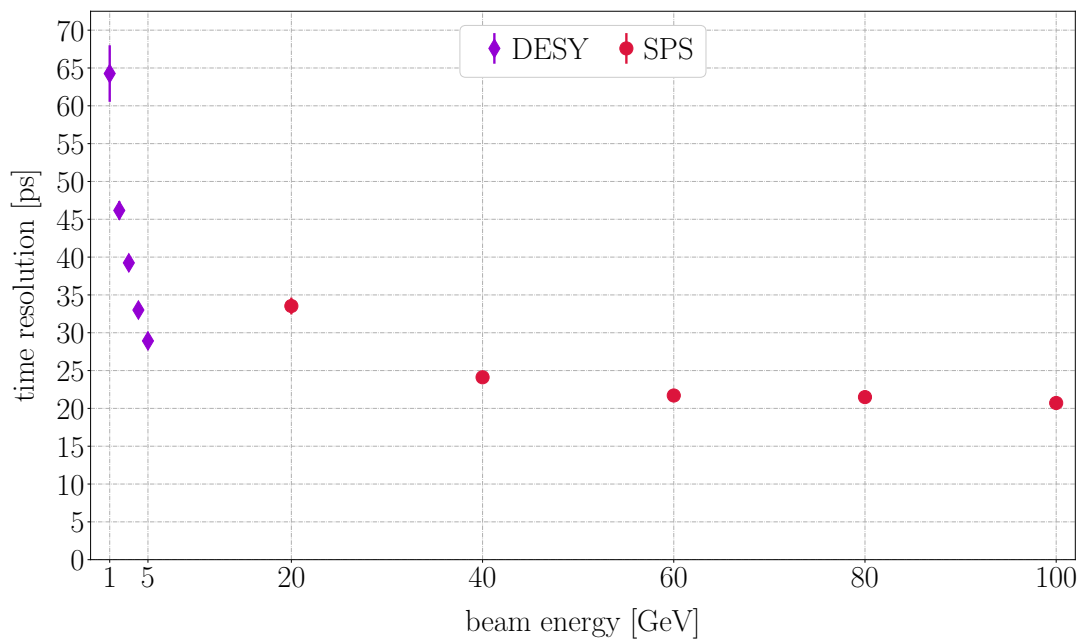


Figure 4.11: Time resolution with respect to energy from 1 to 100 GeV.

4.2.4 Spatial homogeneity of time response

Homogeneity of the response over a larger cell area is an important property of a calorimeter module. This applies to both time resolution and energy resolution. For example, if the time of arrival of a particle hitting the corner of a cell is measured differently compared to when a particle hits the center of the cell, this introduces a spatial dependence of the time measurement on the hit position. In such a case, the time measurement without prior information on the hit position becomes inaccurate, and its time resolution is likely significantly degraded.

Measurements and results - DESY

At DESY, a set of measurements was performed where the beam was centered at eight different positions on the module - the centers of the four cells 6, 7, 10, and 11, the borders between cells 6 and 7, 6 and 10, 7 and 10, and the corner connecting all four cells. With a data set like this, the area of the four cells was more or less evenly covered with the particle beam, and the events could be grouped based on their hit position to create a spatial grid resembling a two-dimensional histogram. By reconstructing the time of events in each bin and finding the mean-time and the time resolution, we can obtain a spatial map of the time response homogeneity as shown in figure 4.12, and separately for each cell in figures 4.13, 4.14, 4.15, and 4.16.

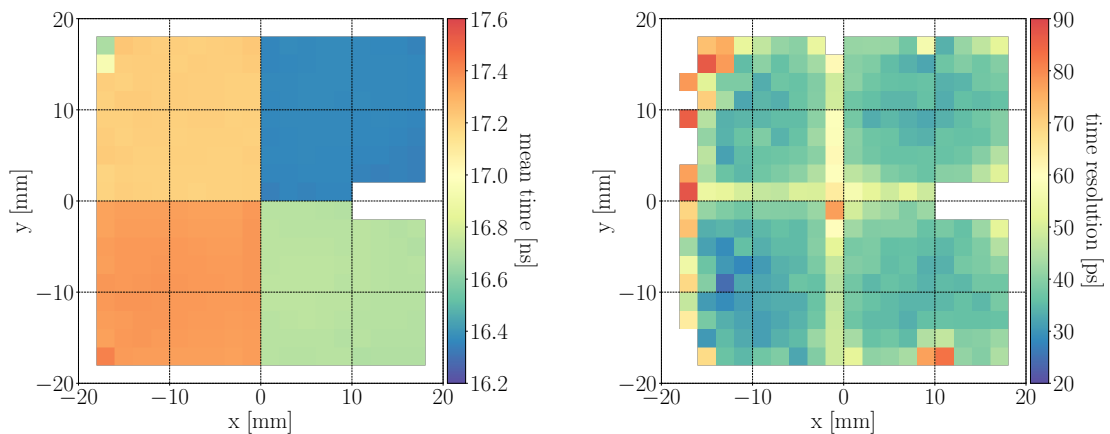


Figure 4.12: (a) Homogeneity map of the reconstructed mean time of the four cells. (b) Homogeneity map of the time resolution of the four cells.

The coordinate system has its origin in the center of the 2×2 matrix, as seen from the front. It means cell 6 sits in the top right corner and cell 11 in the bottom left corner. The x-axis is therefore mirrored compared to figure 4.4.

The four cells have different reconstructed average mean times. It can be due to the rotation of the prototype with respect to the beam, which means that some of the cells are tilted towards the beam pipe and closer to the MCPs that provide the time reference. Other reasons include the differences between the channels of the digitizer, slight variations in the signal cable lengths, and fluctuations in shower propagation and light transport. However, these effects do not negatively impact the time resolution, as shown on the right plot in figure 4.12. The time resolution is relatively flat in the central part of all four cells and starts to degrade when moving out of the cell and toward the cell borders. This is expected and can be explained

by the loss of shower containment within a single cell. At cell borders, the signal is shared between neighboring cells, and fluctuations within a single cell are greater.

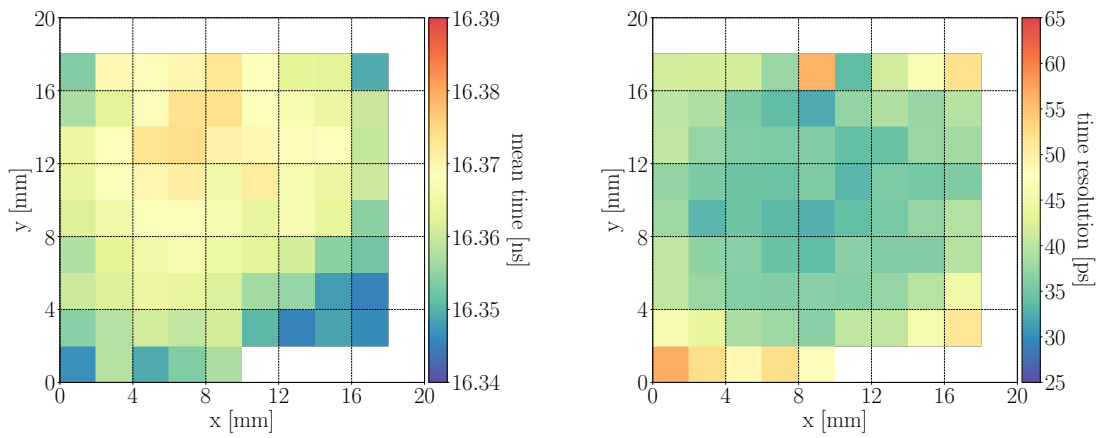


Figure 4.13: (a) Mean time map of cell 6. (b) Time resolution map of cell 6.

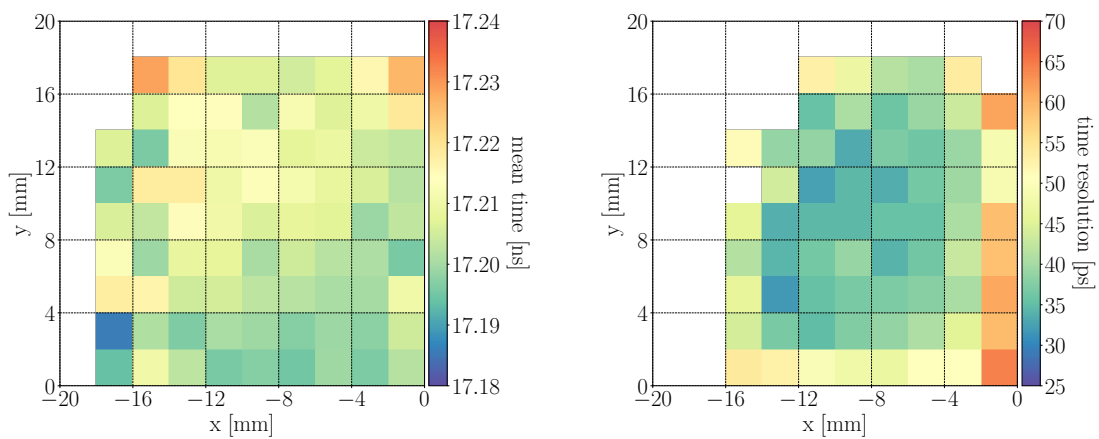


Figure 4.14: (a) Mean time map of cell 7. (b) Time resolution map of cell 7.

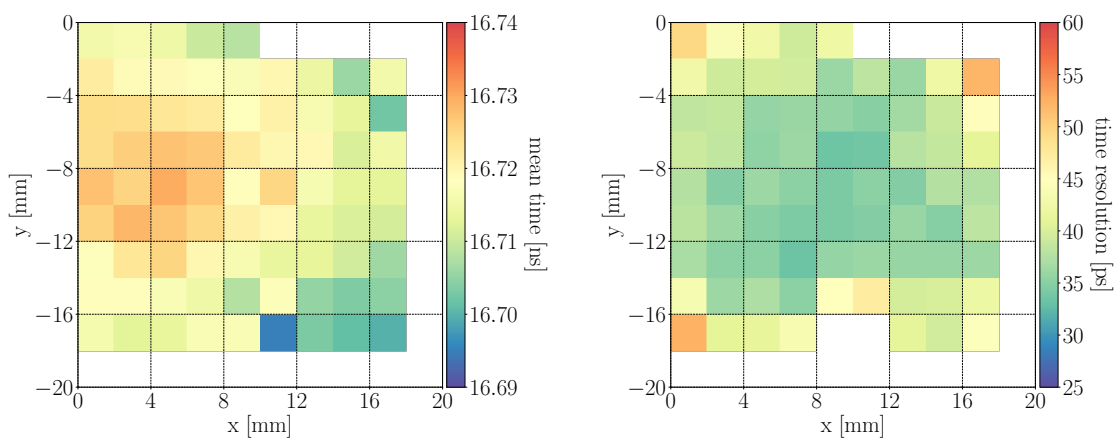


Figure 4.15: (a) Mean time map of cell 10. (b) Time resolution map of cell 10.

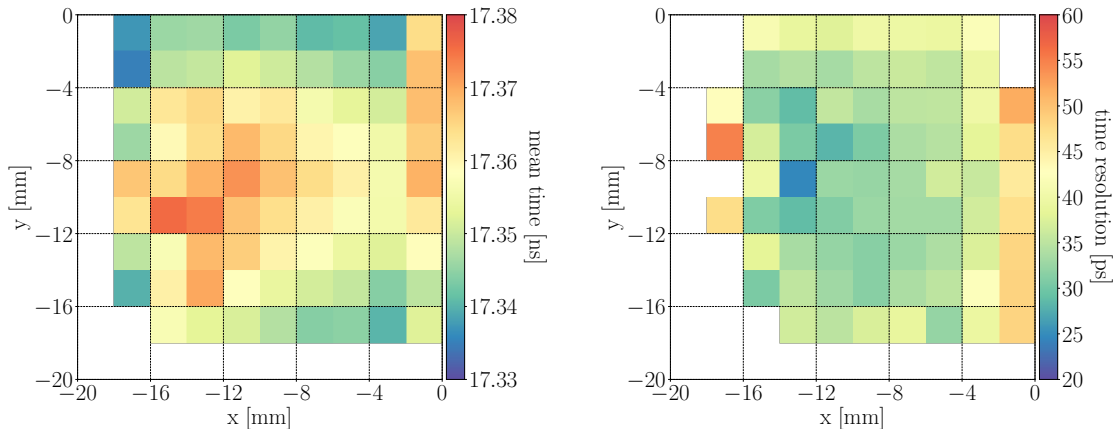


Figure 4.16: (a) Mean time map of cell 11. (b) Time resolution map of cell 11.

Within a single cell, there is no significant drift of the mean time, as can be seen from the color axis of the mean time maps of each of the cells. The time interval the color maps cover is for all cells lower than ~ 60 ps, which means the cells have a uniform time response, and no significant spatial dependence of the reconstructed mean time was observed. The time resolution is better than ~ 30 ps in the center of the cells and starts to degrade when moving to the cell borders. It is interesting to note here that for electrons hitting between two cells, it is possible to recover the loss in time resolution by combining the information from both cells.

4.3 Energy resolution

A step to perform before the energy resolution calculations is the calibration of the cells with respect to one another so that they have an even response to the particles of a given energy. Differences in the response can come from gain fluctuations and different quantum efficiencies of the PMTs paired to each cell. The calibration is done by shooting a single-energy particle beam in the center of each cell, noting down their response (e.g., the average amplitude), and then equalizing it, obtaining the calibration factors, which are then used in the energy reconstruction algorithm.

4.3.1 Energy resolution with respect to inclination angle

A distinctive property of the SpaCal calorimeter is that its energy resolution depends on the angle at which the particles enter the module because the sampling rate depends on it. At the beginning of its development, an electromagnetic shower is transversally narrower than the pitch of a fiber. This gives rise to large differences in energy deposition and longitudinal fluctuations around its starting position, depending on whether the primary electron hits first the absorber or a fiber. Inclining the prototype offers a higher sampling rate along the direction of the primary electron, thus reducing the fluctuations and improving energy resolution. However, this effect fades above inclination angles of 3° in azimuthal and 3° in the altitudinal direction (in short, $3^\circ + 3^\circ$), and the energy resolution approaches its optimum value.

Measurements and results - DESY

At DESY, the energy resolution was measured in the low energy range, from 1 to 5 GeV, shooting the beam in the center of the 4×4 cell matrix. The measurements are shown in figure 4.17 and the results in table 4.1. Since the fit parameters are

correlated, it is hard to give a precise estimation of the three at the same time. This is true, especially for the constant term, which can be better estimated at higher energies. An approach that works relatively well is to assume the noise term is equal for all given inclination angles and perform a common fit of the following. The other two parameters are then fitted for each data subset (i.e., inclination angle), such that the χ^2 of the common fit is minimized, while the noise is kept common to all. The reduced χ^2 , shown in figure 4.18, represents the goodness of the common fit. The estimated value of the noise term at DESY is $(9.6 \pm 0.2)\%$, or 96 MeV at 1 GeV.

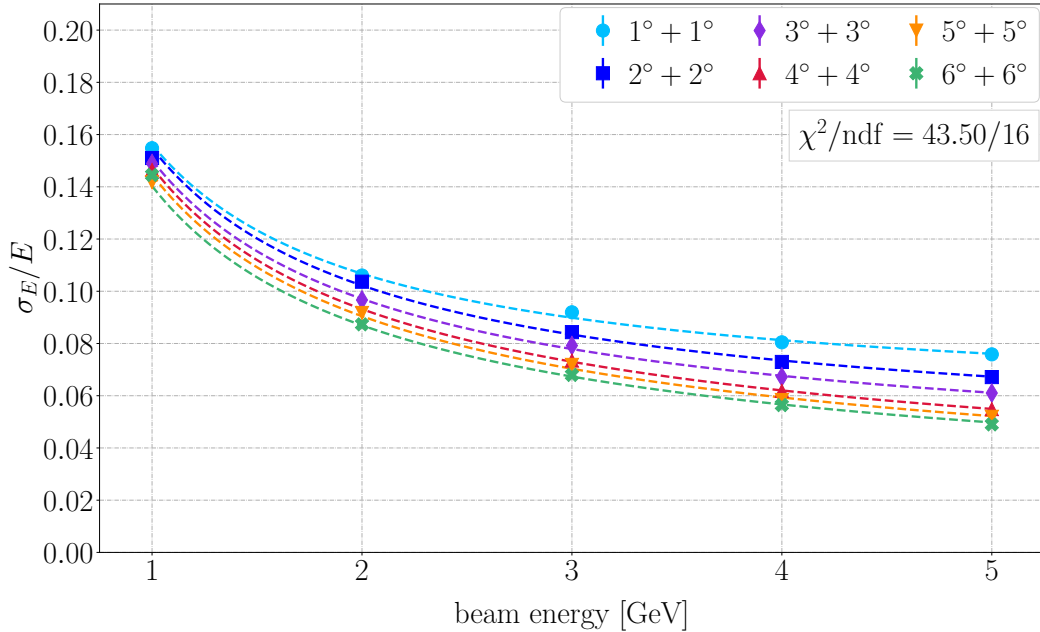


Figure 4.17: Energy resolution measured at DESY.

Table 4.1: The sampling term of the energy resolution measured at DESY.

inclination angle	beam position	sampling term [%]
1° + 1°	center	11.1 ± 0.3
2° + 2°	center	11.6 ± 0.3
3° + 3°	center	11.2 ± 0.2
3° + 3°	cell 11	9.9 ± 0.1
4° + 4°	center	11.2 ± 0.3
5° + 5°	center	10.9 ± 0.1
6° + 6°	center	10.3 ± 0.1

Table 4.1 compares the sampling term of the energy resolution at different inclination angles of the prototype. The errors shown include only the statistical uncertainty of the estimated fit parameters. The systematic error is expected to be much higher, on

the order of 1-2%, as discussed in [20], and providing a reasonable estimation of the constant term therefore becomes difficult. For comparison, a measurement shooting in the center of cell 11 is included, which was done only at an inclination angle of $3^\circ + 3^\circ$. The results give two main conclusions. First, the energy resolution improves by increasing the inclination angle, with the effect fading above $3^\circ + 3^\circ$. At $3^\circ + 3^\circ$ and $6^\circ + 6^\circ$ the sampling terms are $(11.1 \pm 0.2)\%$ and $(10.3 \pm 0.1)\%$, respectively. Second, the sampling term is better when shooting in the center of a selected cell (e.g., cell 11) instead of the center of the 4×4 cell matrix. This can be explained due to effects arising from the light transport, mainly by the geometry of the light guide, which is symmetric with respect to the cell center, and the proximity of the screw hole (i.e., the center of cell 11 is further away from the screw hole than the center of the 4×4 cell matrix), which introduces inhomogeneities in the response.

Measurements and results - SPS

At SPS, the energies, and with that, the number of photons reaching the PMT surface, is almost an order of degrees higher than in DESY. Unfortunately, the Hamamatsu R14755U-100 PMT becomes non-linear in this range of light intensities and in the configuration (HV and signal amplitude range) we used, as can be seen from figure 4.18. A simplistic approach uses response curves to correct for non-linearity. The response is defined as the sum of the amplitudes of the cells used for energy reconstruction divided by the expected energy. In the ideal case, the response remains constant (and equal to one) for all energies. This correction method assumes the main contribution to the amplitude sum comes from a single cell and that the non-linearity can be corrected with a response curve based on the amplitude sum and not on the cell-to-cell basis. A more accurate approach needs non-linearity curves, for example, obtained with the method explained in chapter 3.3.1, for each of the cells (PMTs), and then non-linearity is corrected for each cell individually.

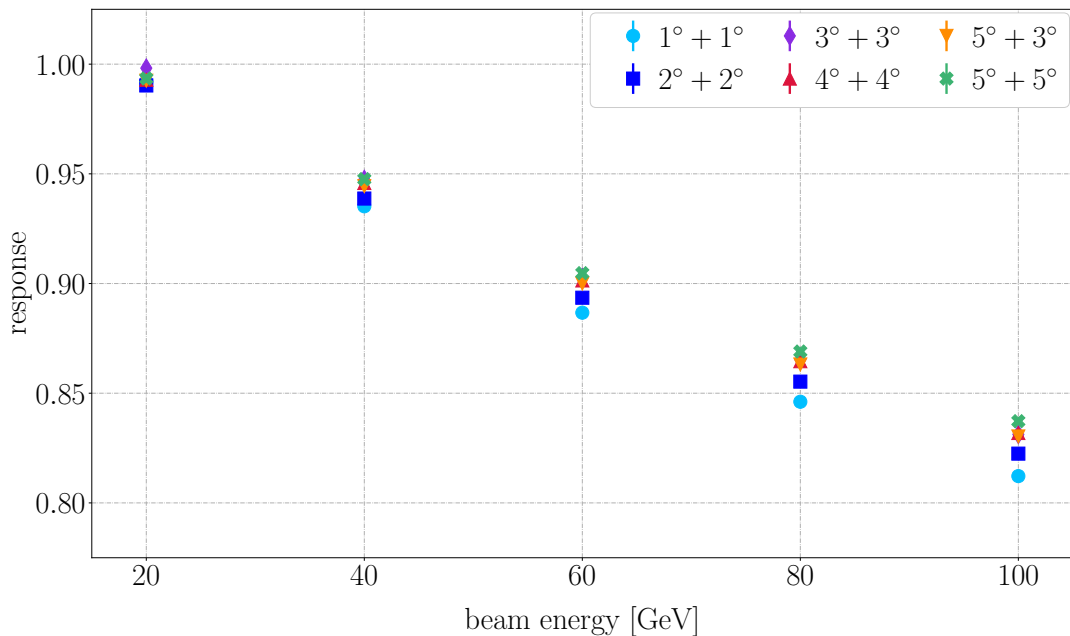


Figure 4.18: Response at different inclination angles of the prototype.

The energy resolution after the non-linearity correction is shown in figure 4.19, and

the results are given in table 4.2. Here, the same method of a common fit of the noise term, as applied to the DESY data, was used. At SPS, the measurements were done by shooting the beam in the center of cell 11 at different inclination angles of the prototype, different from DESY, where only one measurement was done in the center of cell 11 (at $3^\circ + 3^\circ$), and the rest in the center of the 4×4 cell cluster.

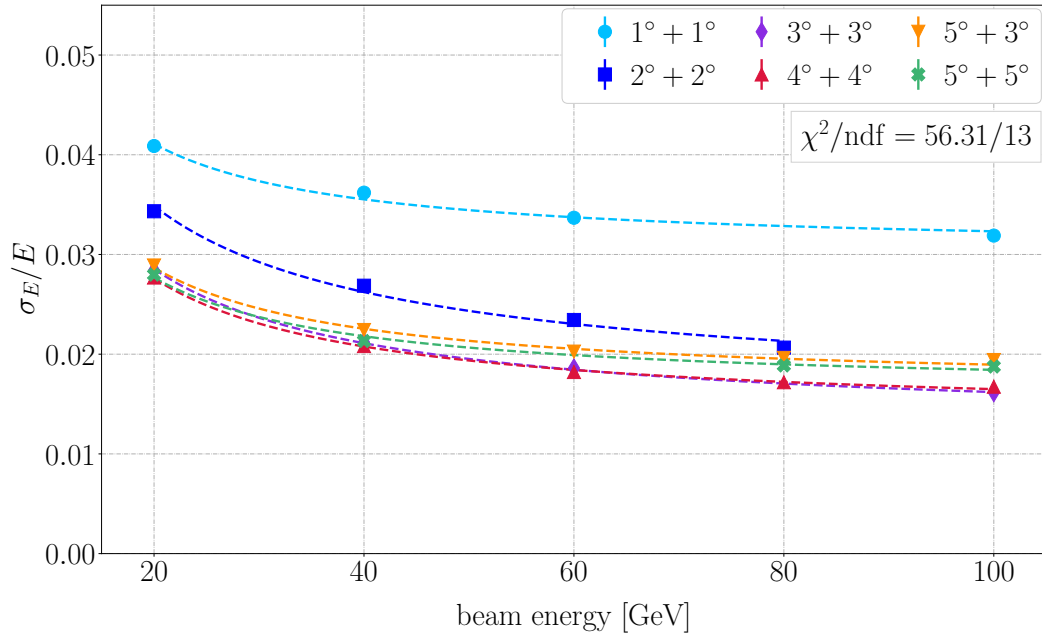


Figure 4.19: Energy resolution measured at SPS.

Table 4.2: The sampling term and constant term of the energy resolution measured at SPS and different inclination angles of the prototype.

inclination angle	sampling term [%]	constant term [%]
$1^\circ + 1^\circ$	11.0 ± 0.4	3.03 ± 0.03
$2^\circ + 2^\circ$	12.7 ± 0.3	1.56 ± 0.04
$3^\circ + 3^\circ$	10.0 ± 0.3	1.25 ± 0.02
$4^\circ + 4^\circ$	9.1 ± 0.4	1.35 ± 0.03
$5^\circ + 3^\circ$	8.8 ± 0.4	1.66 ± 0.03
$5^\circ + 5^\circ$	8.2 ± 0.4	1.63 ± 0.03

At SPS, the energy resolution can be measured at higher energies, and therefore, the evaluation of both the sampling and the constant term is possible. The conclusions are in line with what was shown at DESY. The sampling term improves by increasing the inclination angle of the prototype, and so does the constant term, before the effect saturates at around $3^\circ + 3^\circ$, where the sampling and the constant terms are $(10.0 \pm 0.3)\%$ and (1.25 ± 0.02) , respectively. The errors in the table 4.2 again

include only the statistical uncertainties, while the systematic error is believed to be higher, as seen from the fluctuation of the constant term for the last four presented datasets, but much smaller compared to the one at DESY. For the noise term, the same method of a common fit was used and the estimated value is $(25.5 \pm 2.2)\%$.

4.3.2 Energy resolution at energies from 1 to 100 GeV

For the measurement shooting in the center of cell 11 at $3^\circ + 3^\circ$, I can combine the data measured at DESY and SPS and show the energy resolution over the energy range from 1 to 100 GeV. In this case, the respective noise terms, $(9.6 \pm 0.2)\%$ at DESY and $(25.5 \pm 2.2)\%$ at SPS, have to be subtracted in quadrature from the measurements. Figure 4.20 shows the energy resolution, and the values of the sampling term and the noise term are provided in the legend of the same figure.

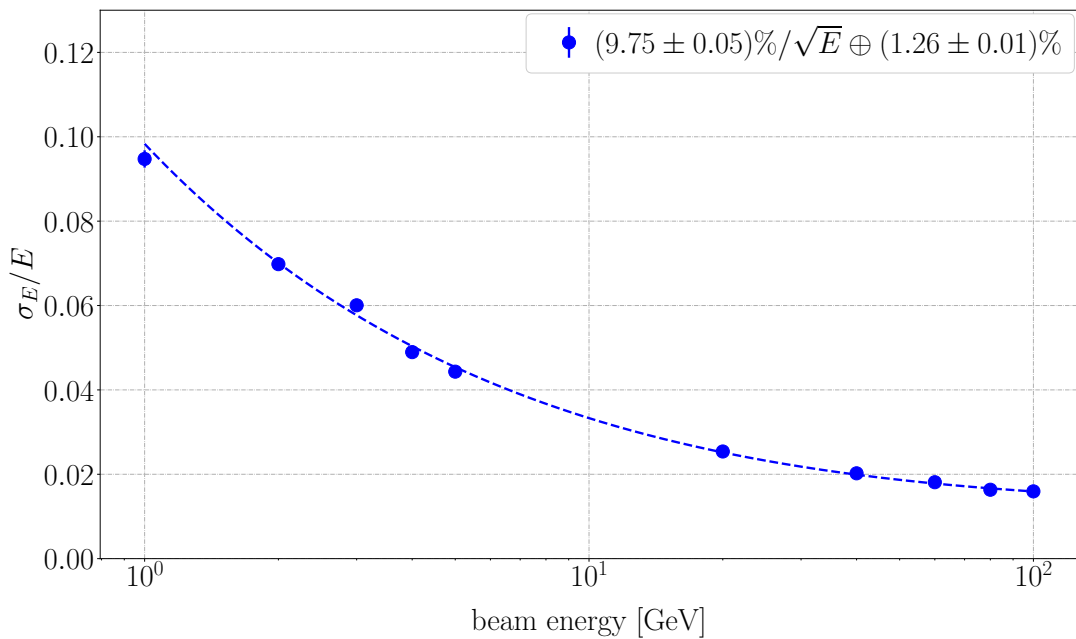


Figure 4.20: Energy resolution measured in the energy range from 1 to 100 GeV.

5. Simulation studies

Simulation studies play an important role in the development of new detector technologies, offering a cost-effective approach to explore various detector geometries and utilize the simulation outcomes to develop new prototypes. Through simulations, we can scale up a single module using measurement data to create a complete detector and evaluate its impact on the physics performance. It is common to compare simulation results with test beam data, either to gain a deeper understanding of inherent uncertainties in measurements or to further improve the simulation framework.

5.1 Simulation framework

The simulation framework used to study the performance of the SpaCal technologies is a Hybrid Monte-Carlo (Hybrid-MC) simulation package [29]. The framework provides full information on the interaction of incident particles with the calorimeter, it allows generation of realistic photodetector pulses and has options for both full or parameterized propagation of optical photons. Ray-tracing of optical photons is useful to study in detail the performance of prototypes, but it comes with significant performance costs. The Hybrid-MC approach, illustrated in figure 5.1, provides a good level of realism while keeping the simulation much faster than full ray-tracing.

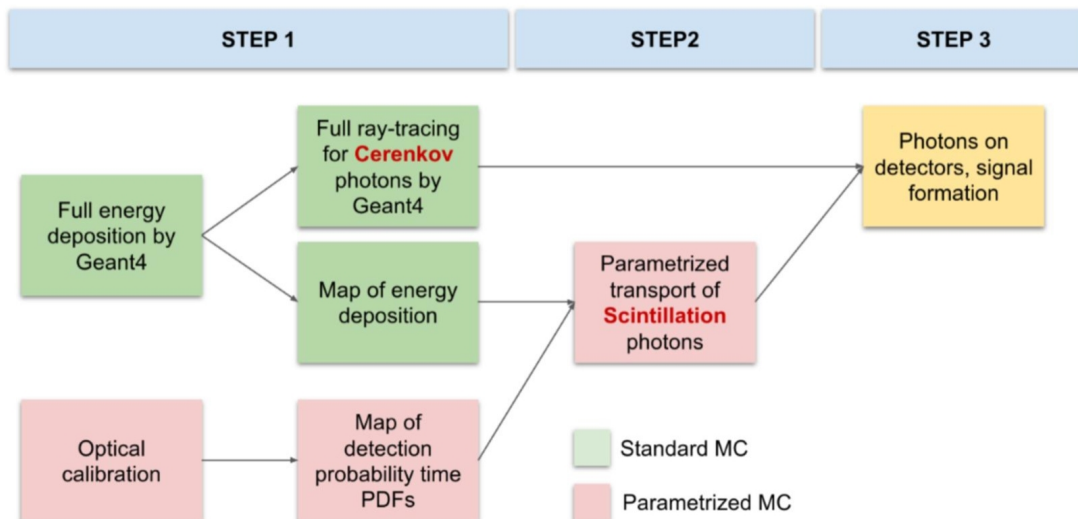


Figure 5.1: Schematics of the Hybrid-MC parametrization strategy [29].

The parametrization strategy of the Hybrid-MC simulations has three step:

- Step 1: Full energy deposition and full ray-tracing of Cherenkov photons by GEANT4 [30]. This step produces a map of energy deposition and tracks the

Cherenkov photons to the detector surface. Additionally, this part includes an optical calibration step, which returns a map of detection time probabilities.

- Step 2: Parametrized transport of scintillation photons.
- Step 3: Propagation of photons on detectors and signal formation.

The Hybrid-MC allows a gain in computation time by two orders of magnitude, and it shows good agreement with both full ray-tracking MC simulations for the photon time distributions and test beam data for the energy resolution.

5.2 Energy resolution of the new SpaCal prototype

The simulation framework supports full ECAL simulations and allows studies of single calorimeter modules. The latter help us better understand the performance of prototypes in test beams by comparing the results with the simulation data. In the simulations below, 4500 electrons were simulated, with different energies from 1 to 100 GeV, entering the new SpaCal prototype through the center of cell 11. The simulations were done for different inclination angles of the prototype, and for the energy reconstruction, the same cluster of 4×4 cells as in chapter 4.3.2, was used. Figure 5.2 shows the energy resolution obtained from the simulations, and table 5.1 gives the values of the sampling term and constant term at different angles.

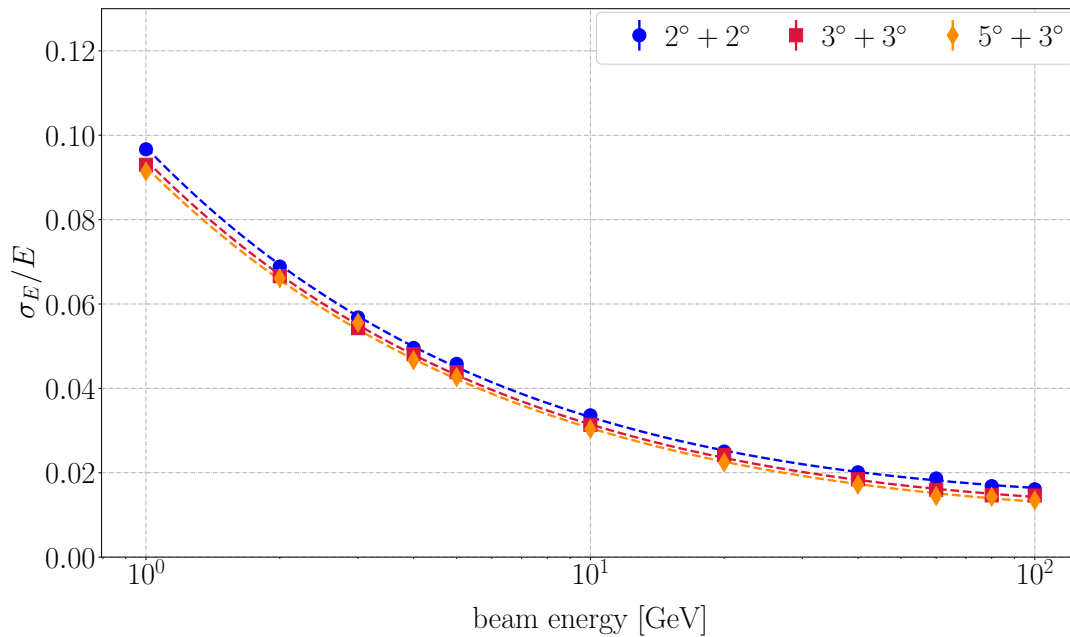


Figure 5.2: Energy resolution in the energy range from 1 to 100 GeV obtained from the simulations at different inclination angles of the prototype.

The simulation results agree with the result obtained from the measurements at different inclination angles of the prototype, in particular, they show an improvement of the energy resolution at higher angles. The sampling term at $3^\circ + 3^\circ$ obtained from simulations is $(9.35 \pm 0.05)\%$, slightly lower than the $(9.9 \pm 0.1)\%$ measured at DESY. While the simulations can be compared to measurements when, in both cases, we are shooting in the center of a cell (e.g., cell 11), the same is not true for

5.2. Energy resolution of the new SpaCal prototype

datasets shooting at a different point on the module (e.g., the center of the 4×4 cell cluster). This is because in the simulation, in such a configuration, the energy resolution will remain unaffected by the effects that otherwise degrade it, such as inhomogeneities in the light transport, because the simulations do not include them.

Table 5.1: The sampling term and constant term of the energy resolution obtained from the simulation at different inclination angles of the prototype.

inclination angle	sampling term [%]	constant term [%]
$2^\circ + 2^\circ$	9.62 ± 0.05	1.33 ± 0.02
$3^\circ + 3^\circ$	9.35 ± 0.05	1.08 ± 0.02
$5^\circ + 3^\circ$	9.20 ± 0.05	0.94 ± 0.02

At SPS, the energy resolution was measured in the same configuration as in simulation (shooting in the center of cell 11) at three different angles, $2^\circ + 2^\circ$, $3^\circ + 3^\circ$ and $5^\circ + 3^\circ$. While the measurement of the sampling term at $2^\circ + 2^\circ$ shows a much higher value compared to the simulations, the measurements at the other two angles agree with the values obtained from the simulations. The constant term in simulations shows the same improving trend with increasing the inclination angle as observed from the measurements at SPS. At $3^\circ + 3^\circ$, the given values are $(1.25 \pm 0.02)\%$ and $(1.08 \pm 0.02)\%$ for the measurements and simulations, respectively.

5.2.1 Comparison in the energy range from 1 to 100 GeV

Measurements with a common fit of the energy resolution, over the energy range from 1 to 100 GeV, can be compared to simulations at $3^\circ + 3^\circ$, where we have test beam data shooting in the center of cell 11 measured both at DESY and SPS. For the other inclination angles, the data taken at DESY, shooting in the center of cell 11, is missing. Table 5.2 and figure 5.3 show a good agreement between the test beam and simulation data, with the simulation results being slightly better. The latter can be explained by uncertainties present in the measurements but being excluded from the simulations, for example, the calibration factors for the energy reconstruction can be misevaluated, while in the simulations, every cell has an ideal (and equal) response, and so, the calibration factors can be without error set to one.

Table 5.2: Comparison of the sampling and constant term of the energy resolution between simulations and measurements in the energy range from 1 to 100 GeV.

inclination angle	data type	sampling term [%]	constant term [%]
$3^\circ + 3^\circ$	measurements	9.75 ± 0.05	1.26 ± 0.01
$3^\circ + 3^\circ$	simulations	9.35 ± 0.05	1.08 ± 0.02

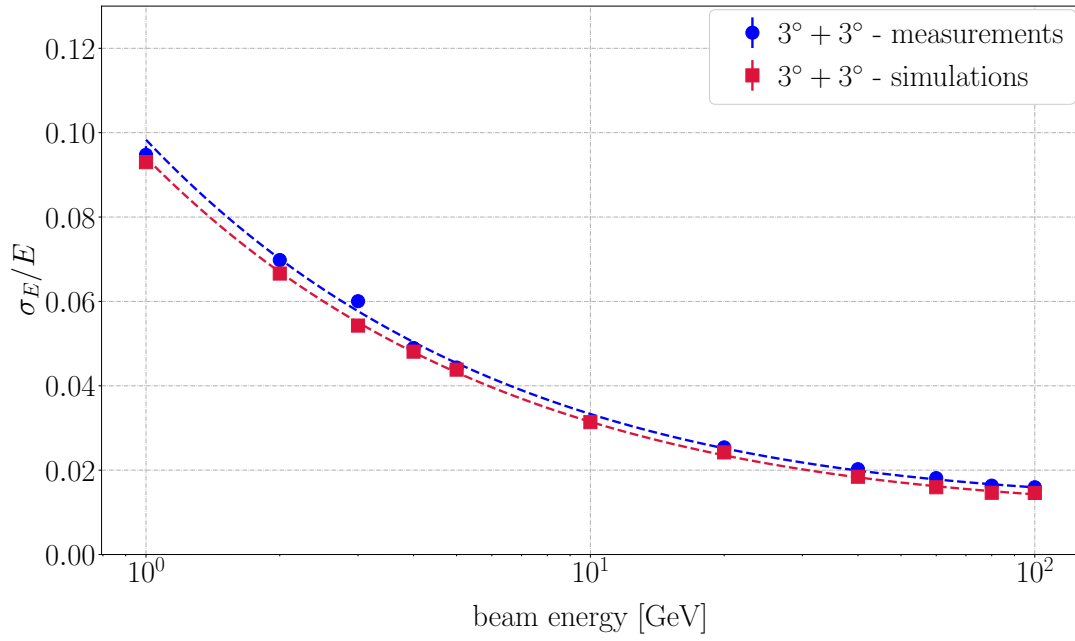


Figure 5.3: Comparison of the measured energy resolution with simulations.

6. Conclusion

The aim of this Master's Thesis was to study the performance of a new "spaghetti calorimeter (SpaCal)" prototype with a tungsten absorber and plastic scintillating fibers. My work was a part of LHCb Upgrade II activities, and I participated in test beam campaigns and assisted with the development of new SpaCal prototypes.

The production of a module-size SpaCal prototype with a tungsten absorber and plastic scintillating fibers included several steps, which took around two months to complete. First, the fibers of the right length had to be prepared and inserted inside the 5184 holes of the 3D-printed tungsten absorber. Next, the fibers were glued together and had their ends polished. Afterward, the prototype was equipped with the remaining pieces: hollow light guide, photomultiplier tubes (PMTs), each having its own voltage divider board, and a calibration system, which required the removal of one scintillating fiber per cell and replacement of it with a clear fiber. The new module-size prototype is 19 cm long, corresponding to $25 X_0$, and $121 \times 121 \text{ mm}^2$ in cross-section, giving home to 36 cells of the SpaCal WPoly modules.

A method to measure response non-linearity of PMTs was developed. It includes a pair of LEDs operating in pulse mode, seated on top of a linear translation stage. By changing the position of the LEDs with respect to the PMT, the amount of light incident on the PMT can be adjusted, following the inverse square law. It was shown that the current experimental setup can achieve the precision of the non-linearity measurement of around 2%, limited mainly by the time-dependent LED fluctuations.

The main results of the two test beam campaigns at DESY and SPS are divided into time resolution measurements and energy resolution measurements. The prior show, the new prototype can achieve $\sim 30 \text{ ps}$ time resolution at 5 GeV and $\sim 20 \text{ ps}$ at 100 GeV electron beam energy. A further study on time resolution showed uniformity of time response over a large cell area, with increasing degradation when moving towards the cell borders, which can be explained, due to the decrease of shower containment within the cell. This leads to greater signal fluctuations and deteriorates the time resolution. However, in this case, the time performance can be recovered by combining the information from the two cells. Regarding energy resolution, an important parameter to study was the inclination of the prototype with respect to the beam direction. This study confirmed what was already shown in [20], that the energy resolution of SpaCal prototypes improves with higher inclination angles, however, the improvement starts to saturate after inclination of 3° in the azimuthal and 3° in the altitudinal direction. At $3^\circ + 3^\circ$ the energy resolution of the new prototype is $\sim 9.75\%/\sqrt{E} \oplus 1.26\%$ in the energy range from 1 to 100 GeV.

Last, a brief comparison between the test beam results and simulation data shows good agreement between the measurements and simulations. Slight differences could be due to inhomogeneities in the prototype, but not considered in the simulations, impurities in the beam, and small differences in the assumed tungsten density.

7. Bibliography

- [1] *The Large Hadron Collider* / CERN, <https://home.cern/science/accelerators/large-hadron-collider> [accessed 2. 6. 2023].
- [2] *High-Luminosity LHC*, <https://home.cern/science/accelerators/high-luminosity-lhc> [accessed 2. 6. 2023].
- [3] *LHCb Experiment*, <https://home.cern/science/experiments/lhcb> [accessed 7. 6. 2023].
- [4] LHCb collaboration, *The LHCb upgrade I* (2023), arXiv:2305.10515 [hep-ex] .
- [5] LHCb Collaboration, *Framework TDR for the LHCb Upgrade II - Opportunities in flavour physics, and beyond, in the HL-LHC era*, Tech. Rep. (CERN, Geneva, 2021).
- [6] C. W. Fabjan and F. Gianotti, *Calorimetry for particle physics*, Rev. Mod. Phys. **75**, 1243 (2003).
- [7] I. B. Claus Grupen, *Handbook of Particle Detection and Imaging* (Springer Berlin, Heidelberg, 2012).
- [8] H. Kolanoski and N. Wermes, *Particle Detectors* (Oxford University Press, 2020).
- [9] L. Martinazzoli, *Development of a Sampling Calorimeter for the LHCb Upgrade*, Ph.D. thesis, Università degli Studi di Milano-Bicocca (2023).
- [10] W. R. Leo, *Techniques for Nuclear and Particle Physics Experiments*, 2nd ed. (Springer Berlin, Heidelberg, 1994).
- [11] R. L. Workman and Others (Particle Data Group), *Review of Particle Physics*, PTEP **2022**, 083C01 (2022).
- [12] F. H. Attix, *Introduction to Radiological Physics and Radiation Dosimetry* (John Wiley & Sons, Ltd, 1986).
- [13] L. Martinazzoli, N. Kratochwil, S. Gundacker and E. Auffray, *Scintillation properties and timing performance of state-of-the-art Gd₃Al₂Ga₃O₁₂ single crystals*, Nuclear Instruments and Methods in Physics Research Section A: Accelerators, Spectrometers, Detectors and Associated Equipment **1000**, 165231 (2021).

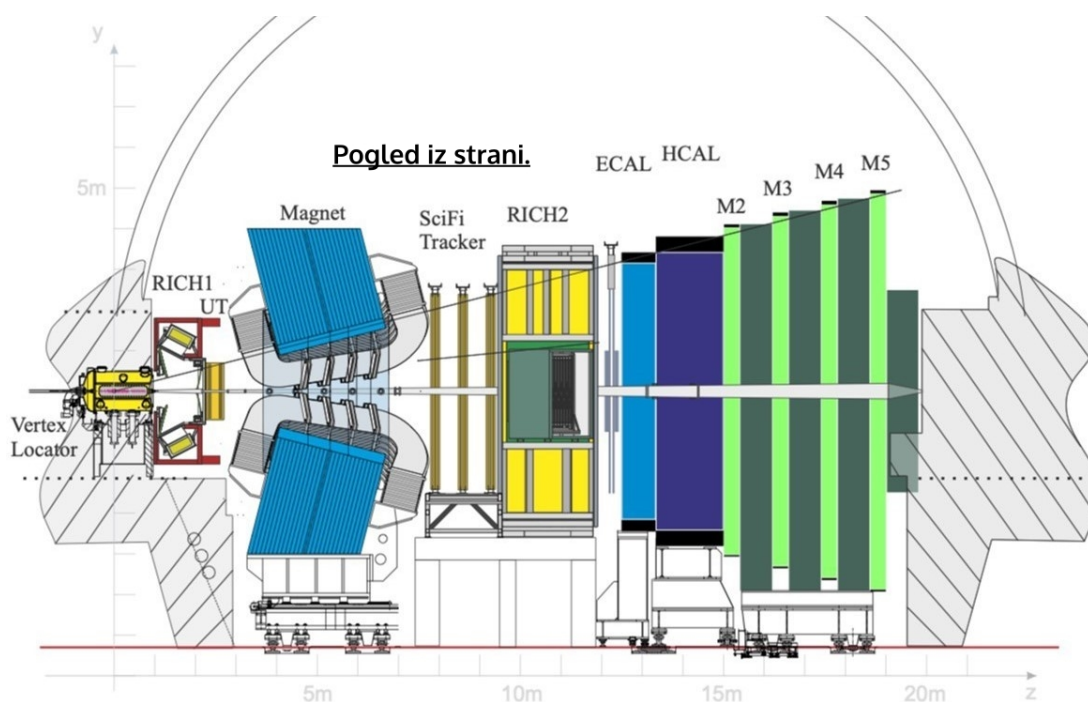
- [14] V. Alenkov, O. Buzanov, G. Dosovitskiy, V. Egorychev, A. Fedorov, A. Golutvin, Y. Guz, R. Jacobsson, M. Korjik, D. Kozlov, V. Mechinsky, A. Schopper, A. Semennikov, P. Shatalov and E. Shmanin, *Irradiation studies of a multi-doped Gd₃Al₂Ga₃O₁₂ scintillator*, Nuclear Instruments and Methods in Physics Research Section A: Accelerators, Spectrometers, Detectors and Associated Equipment **916**, 226 (2019).
- [15] Hamamatsu Photonics K.K., *Photomultiplier Tubes: Basics and Applications* (2017).
- [16] *Hamamatsu - Photomultiplier tubes (PMTs)*, <https://www.hamamatsu.com/jp/en/product/optical-sensors/pmt.html> [accessed 13. 6. 2023].
- [17] *Kuraray - Plastic scintillating fibers (PSF)*, <https://www.kuraray.com/products/psf> [accessed 13. 6. 2023].
- [18] LHCb Collaboration, *The LHCb Detector at the LHC*, Journal of Instrumentation **3** (08), S08005.
- [19] *Longer term LHC schedule*, <http://lhc-commissioning.web.cern.ch/schedule/LHC-long-term.htm> [accessed 22. 6. 2023].
- [20] L. An, E. Auffray, F. Betti, F. Dall’Omo, D. Gascon, A. Golutvin, Y. Guz, S. Kholodenko, L. Martinazzoli, J. M. D. Cos, E. Picatoste, M. Pizzichemi, P. Roloff, M. Salomoni, D. Sanchez, A. Schopper, A. Semennikov, P. Shatalov, E. Shmanin, D. Strelalina and Y. Zhang, *Performance of a spaghetti calorimeter prototype with tungsten absorber and garnet crystal fibres*, Nuclear Instruments and Methods in Physics Research Section A: Accelerators, Spectrometers, Detectors and Associated Equipment **1045**, 167629 (2023).
- [21] S. Kholodenko (LHCb ECAL UII working group), *LHCb ECAL upgrade II*, PoS **PANIC2021**, 100 (2022).
- [22] LHCb Collaboration, *Enhancement of the LHCb ECAL during LS 3 - Technical Design Report*, Tech. Rep. (CERN, Geneva, 2023).
- [23] *EOS GmbH*, <https://www.eos.info/en> [accessed 18. 6. 2023].
- [24] *Huntsman - Araldite 2011*, <https://www.huntsman.com/products/araldite2000/araldite-2011> [accessed 7. 9. 2023].
- [25] *Hamamatsu R14755U-100*, https://www.hamamatsu.com/eu/en/product/optical-sensors/pmt/pmt_tube-alone/metal-package-type/R14755U-100.html [accessed 7. 9. 2023].
- [26] *ICCUB Barcelona*, <https://icc.ub.edu/> [accessed 7. 9. 2023].
- [27] S. Ritt, *Design and performance of the 6 GHz waveform digitizing chip DRS4*, in *2008 IEEE Nuclear Science Symposium Conference Record* (2008) pp. 1512–1515.
- [28] *Hamamatsu R7899*, https://www.hamamatsu.com/jp/en/product/optical-sensors/pmt/pmt_tube-alone/head-on-type/R7899.html [accessed 8. 9. 2023].

-
- [29] M. Pizzichemi, *Scintillating sampling ECAL technology for the Upgrade II of LHCb*, in *Proceedings of the Vienna Conference on Instrumentation* (2022).
- [30] Geant4 Collaboration, *Geant4—a simulation toolkit*, Nuclear Instruments and Methods in Physics Research Section A: Accelerators, Spectrometers, Detectors and Associated Equipment **506**, 250 (2003).

Razširjeni povzetek v slovenskem jeziku

Veliki hadronski trkalnik (LHC) je največji pospeševalnik delcev na svetu, lociran na Švicarsko-Francoski meji blizu Ženeve. Znotraj krožnega pospeševalnika z obsegom okoli 27 kilometrov krožita dva snopa delcev s hitrostjo blizu hitrosti svetlobe, nato pa trčita na štirih mestih okrog obroča, kateri ustrezajo štirim velikim detektorjem delcev - ATLAS, CMS, ALICE in LHCb.

Eksperiment LHCb (Large Hadron Collider beauty) je eden izmed štirih velikih detektorjev, zgrajenih okoli pospeševalnika LHC v Evropskem laboratoriju za fiziko delcev - CERN. Njegov glavni namen je iskanje nove fizike s preučevanjem kršitve CP simetrije in redkih razpadov hadronov s težkimi kvarki. Detektor je naprej-usmerjen spektrometer, ki zaznava delce, izsevane znotraj območja pseudorapidnosti $2 < \eta < 5$. Detektorski podsistemi, ki ga sestavljajo, so glede na svojo primarno vlogo deljeni na sistem za sledenje delcev (angl. *tracking*) in sistem za identifikacijo delcev (angl. *particle identification*). Del prvega sistema so detektor za rekonstrukcijo točke trka VELO (VERTex LOcator) in dva detektorja za rekonstrukcijo sledi nabitih delcev - UT (Upstream Tracker), nameščen pred magnetom, in SciFi (Scintillating Fibre), postavljen za magnetom. Sistem za identifikacijo delcev vsebuje dva detektorja obročev Čerenkova (RICH1 in RICH2), kjer vsak izmed njih pokriva del spektra gibalnih količin, elektromagnetni kalorimeter (ECAL) za meritev energije elektronov, pozitronov in visoko-energijskih fotonov, hadronski kalorimeter (HCAL) prvotno zasnovan za namen proženja in mionske komore za detekcijo mionov. Trenutni detektor, prikazan na sliki 1, bo zbiral podatke do konca leta 2025, potem pa nastopi tri-letno obdobje, znotraj katerega se bo nadgradilo določene detektorske sisteme, kot del priprave na prihajajoči dvig luminoznosti iz trenutnih $2 \times 10^{33} \text{ cm}^{-2} \text{ s}^{-1}$ na $1.5 \times 10^{34} \text{ cm}^{-2} \text{ s}^{-1}$, kar predstavlja povečanje za faktor 7.5-krat.



Slika 1: Shematski stranski pogled detektorja LHCb. Povzeto po [4].

Kalorimetrija

Kalorimetrija je splošno razširjen princip detekcije v fiziki osnovnih delcev. Metoda je bila prvotno zasnovana za preučevanje pojavov s kozmičnimi žarki in kasneje prilagojena za uporabo v eksperimentih na pospeševalnikih, predvsem za merjenje energije elektronov, fotonov in hadronov. Tradicionalno so kalorimetri sestavljeni iz blokov materiala, v katerem se delci popolnoma absorbirajo in se njihova energija pretvori v merljivo količino, kot je na primer scintilacijska svetloba.

Kalorimetre v splošnem delimo na elektromagnetne kalorimetre, ki se uporabljajo predvsem za merjenje energije elektronov in fotonov, in hadronske kalorimetre, ki se uporabljajo predvsem za merjenje energije hadronov. Glede na konstrukcijsko tehniko jih lahko dalje razvrstimo na vzorčevalne kalorimetre in homogene kalorimetre.

Vzorčevalni kalorimeter sestavljajo izmenjujoče plasti pasivnega in aktivnega medija. Pasivna plast je material z visoko zavorno močjo, torej velikim atomskim številom, kot so svinec, železo ali baker. Aktivna plast vzorči deponirano energijo. Pogosto so to scintilatorji, ki pretvorijo ionizacijske izgube v scintilacijsko svetlobo.

Scintilacijski detektorji

Detektorji, ki temeljijo na detekciji scintilacijskih fotonov, niso namenjeni izključno kalorimetrom in se širše uporabljajo pri zaznavanju sevanja. Ti detektorji pretvarjajo energijo vpadnih delcev v scintilacijsko svetlobo, ki se nato pretvori v električni impulz. Običajno jih sestavljata dve osnovni komponenti: scintilator in fotodetektor.

Scintilacija je vrsta luminiscence, ki jo povzroči ionizirajoče sevanje v dielektričnih medijih. Po vzbuditvi luminiscenčnih centrov se ti relaksirajo z emisijo fotonov.

Takšni materiali so znani kot scintilatorji in jih na splošno razdelimo v dve skupini: anorganske in organske scintilatorje. Anorganski scintilatorji imajo ponavadi višji svetlobni pridelek, višjo moč ustavljanja (angl. *stopping power*), predvsem na račun višje gostote in so običajno manj občutljivi na sevanje. Po drugi strani, so organski scintilatorji cenejši in imajo krajše scintilacijske čase ter so zato hitrejši.

Pri večini fotodetektorjev poteka detekcija fotonov v treh korakih. Najprej vpadni foton ustvari primarni fotoelektron oziroma par elektron-vrzel preko fotoelektričnega ali fotoprevodnega pojava. V drugem koraku se s pomnoževanjem, število elektronov poveča na zaznavno raven, tako da v tretjem koraku pomnoženi elektroni proizvedejo električni signal. Fotopomnoževalke, struktura elektrod v steklenem ohišju z vakuumom, so popularen tip fotodetektorja. Foton na fotokatodi izbije elektron, kateri se pomnoži v strukturi elektrod. Oblak sekundarnih elektronov se zbere na zadnji elektrodi, anodi, in proizvede električni signal. Fotopomnoževalke so primerne za uporabo v kalorimetriji, saj imajo linearni odziv znotraj relativno širokega območja intenzitet svetlobe, omogočajo natančno meritev časa prihoda scintilacijskih fotonov in so manj občutljive na sevanje v primerjavi s polprevodniškimi fotodetektorji.

Kalorimetska tehnologija SpaCal

Špagetni kalorimeter (angl. *Spaghetti calorimeter*) SpaCal je kalorimetska tehnologija pri kateri so scintilacijska vlakna vstavljena v odprtine gostega absorberja. V primerjavi z bolj tradicionalno tehnologijo Šašlik, ne uporablja pretvornikov valovne dolžine (angl. *wavelength shifter*), kateri običajno ne vzdržijo močnega obsevanja in pokažejo nesprejemljivo degradacijo po obsevanju nad 40 kGy. Iz tega razloga je SpaCal primeren kandidat pri nadgradnji II elektromagnetnega kalorimetra LHCb eksperimenta (ECAL), po kateri se pričakuje zajemanje podatkov pri bistveno višji luminoznosti. To implicira višjo obsevanost in zahteva od kalorimetskih modulov, postavljenih najbližje interakcijski osi, sevalno vzdržljivost do 1 MGy.

SpaCal prototip z volframovim absorberjem

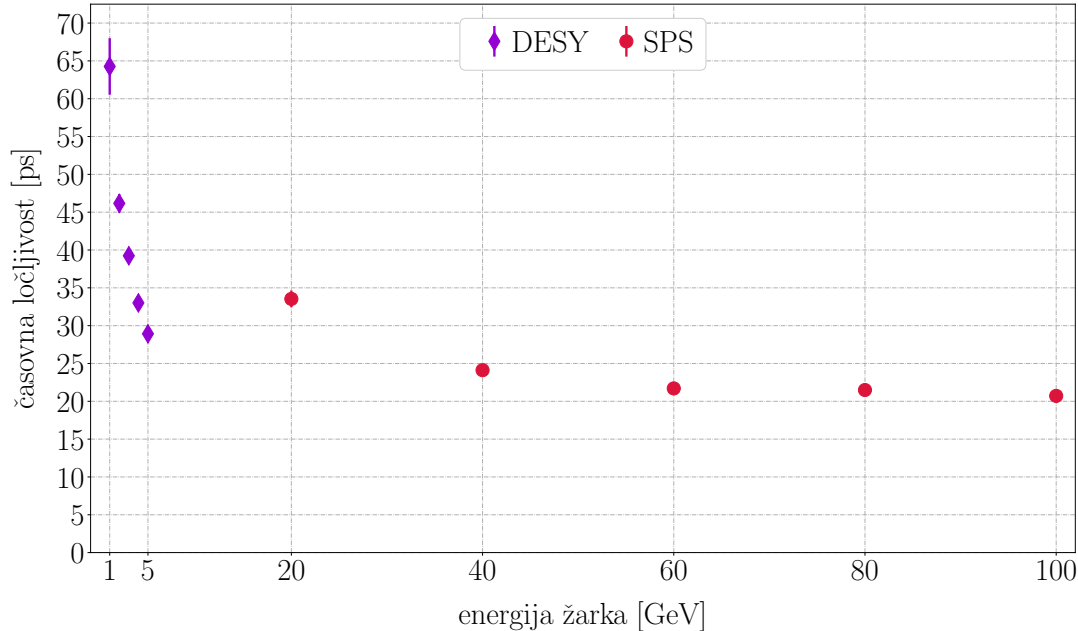
Izhodiščna rešitev nadgradnje ECAL vključuje zamenjavo trenutnih Šašlik modulov v osrednji regiji s SpaCal moduli z volframovim absorberjem. Po načrtovani nadgradnji med LS3 (angl. *Long Shutdown 3*), ta vključuje uporabo SpaCal modulov z volframovim absorberjem in plastičnimi scintilacijskimi vlakni, med LS4 (angl. *Long Shutdown 4*), pa se bo ta nadomestilo z GAGG kristalnimi vlakni, saj so manj občutljiva na sevanje, in ponovno uporabo obstoječih absorberjev.

Izdelava SpaCal prototipa z volframovim absorberjem je vključevala naslednje korake: razvoj in proizvodnjo mehaničnih kosov, rezanje scintilacijskih vlaken, vstavitve scintilacijskih vlaken v absorber, lepljenje scintilacijskih vlaken, poliranje scintilacijskih vlaken, razvoj in namestitve kalibracijskega sistema, razvoj in proizvodnjo votlih vodnikov svetlobe, razvoj in proizvodnjo nosilcev za fotodetektorje, karakterizacijo ploščic z delilnikom napetosti, in namestitve fotodetektorjev. Novi SpaCal prototip smo maja testirali na pospeševalniku inštituta DESY s testnim žarkom pospešenih elektronov energij od 1 do 5 GeV, kasneje julija pa še v CERN-u na pospeševalniku SPS s testnim žarkom energij od 20 do 100 GeV. Na podlagi zajetih podatkov smo prototipu določili njegovo časovno in energijsko ločljivost.

Časovna ločljivost

Standardni pristop za določitev časovne ločljivosti je prilagajanje funkcije podatkom. V histogram se za vsak dogodek vnaša razlika med časom, ki ga izmerita prototip in referenčni detektor. Iz postopka prilagajanja se dobi vrednost standardne deviacije, kot parameter prilagojene Gaussove funkcije. Ta, po odštetju prispevka reference v kvadratu, predstavlja časovno ločljivost testirane količine. V naši eksperimentalni postavitvi znaša prispevek referenčnega detektorja $\sim 15\text{-}20$ ps.

Od energijske odvisnosti se pričakuje izboljšanje časovne ločljivosti pri višjih energijah, kar gre na račun boljše fotostatistike in posledično manjših fluktuacij v obliki signala. To velja do neke meje, nad katero začnejo v časovni ločljivosti dominirati ostali prispevki, na primer razpadni čas scintilatorija in časovna ločljivost fotodetektorja. Z zajemom polnih oblik signala se lahko za rekonstrukcijo časa uporabi metoda konstantne frakcije (angl. *constant fraction discrimination*), pri kateri se odčita čas pri prehodu signala nad določenim odstotkom maksimalne amplitude. Izkáže se, da izbira praga ni trivialna in se lahko z izbiro optimalne vrednosti izboljša časovna ločljivost. Optimalna vrednost se lahko eksperimentalno določi in je v našem primeru znašala 20% v DESY-ju in 75% v SPS-u. Podobno velja tudi za izbiro optimalne delovne napetosti fotopomoževalk. Za celico prototipnega modula, katere rezultati so prikazani na sliki 2, je bila izbrana optimalna napetost v DESY-ju 650 V in v SPS-u 450 V. Po optimizaciji obeh parametrov je bila izmerjena časovna ločljivost v DESY-ju ~ 30 ps pri 5 GeV, in v SPS-u ~ 20 ps pri 100 GeV.



Slika 2: Časovna ločljivost pri energijah od 1 do 100 GeV.

Energijska ločljivost

Pri določanju energijske ločljivosti kalorimetra se na podatke prilagaja funkcija:

$$\frac{\sigma}{E} = \frac{a}{\sqrt{E}} \oplus \frac{b}{E} \oplus c \quad (1)$$

V tem vrstnem redu, so prispevki v enačbi - vzorčevalni člen (angl. *sampling term*), člen šuma (angl. *noise term*) in konstantni člen (angl. *constant term*).

V homogenih kalorimetrih so fluktuacije meritve deponirane energije majhne, zato ker material, ki gradi kalorimeter, hkrati igra vlogo pasivnega in aktivnega medija, in se deponirana energija vzorči po celotnem volumnu. Nasprotno, je pri vzorčevalnih kalorimetrih del energije za kalorimeter neviden. To bistveno prispeva k fluktuacijam izmerjene energije iz dogodka v dogodek in se izraža v vzorčevalnem členu energijske ločljivosti, ki običajno zavzema vrednosti v velikostnem redu nekaj 10%.

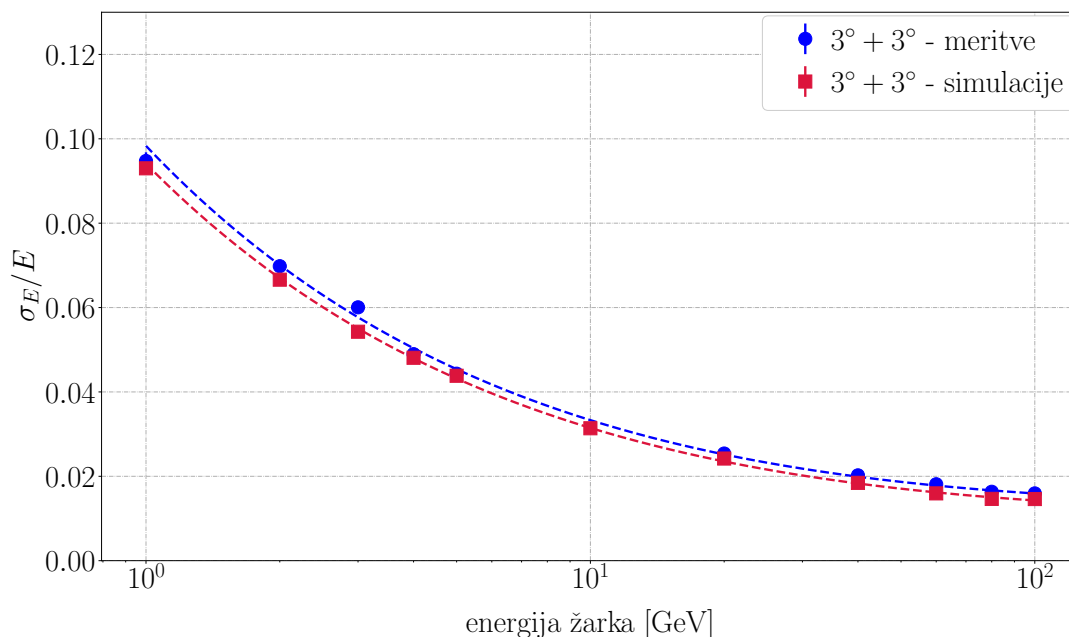
Člen šuma vključuje prispevke bralne elektronike, njegov velikostni red pa določa detekcijska tehnika. V primeru scintilacijskih detektorjev v kombinaciji z detektorji svetlobe, ki signal ojačajo, na primer fotopomnoževalke, je ta člen relativno nizek.

Konstantni člen, kot pove že ime, ostaja neodvisen od energije vpadnega delca. Prisoten je zaradi instrumentalnih učinkov, kot sta na primer neučinkovitost kolekcije signala in mehanske omejitve. Kadar je odziv kalorimetra odvisen od točke vpada delca, torej nehomogen, je meritev energije dodatno razmazana pri meritvah po večjem detekcijskem volumnu. Pogost vir nehomogenosti odziva so nepravilnosti oblike absorberja in aktivne plasti, neenakomerna pokritost, kot so razpoke in mrtva območja znotraj kalorimetra, spremembe odziva zaradi temperaturnih gradientov in učinki zaradi radiacijskih poškodb in staranja detektorja. Te učinke je sicer mogoče korigirati, če imajo periodično pojavljanje oziroma jih je mogoče predvideti.

Parameter, kateri pomembno vpliva na energijsko ločljivost SpaCal prototipov, je orientacija prototipa glede na vpadno smer žarka pospešenih delcev. Pričakuje se, da bo ločljivost izboljšana, če delci vpadajo pod kotom glede na scintilacijska vlakna in ne vzdolžno z njimi. Vendar, ni potrebno, da so koti vpada znatni, saj energijska ločljivost doseže optimalno vrednost oziroma ta efekt začne pojemati že pri rotaciji za $3^\circ + 3^\circ$, torej 3° v altitudni smeri in 3° v azimutalni smeri glede na žarek pospešenih delcev. Tabela 1 povzema rezultate energijske ločljivosti pridobljene iz simulacij pri treh kotih rotacije prototipa, in primerjavo izmerjene vrednosti vzorčevalnega člena in konstantnega člena pri $3^\circ + 3^\circ$. Slika 3 prikazuje primerjavo meritve energijske ločljivosti pri kotu naklona prototipa $3^\circ + 3^\circ$ s simulacijami. Od meritev je odštet prispevek šuma, in sicer posebej za nižje energijsko območje (meritve v DESY-ju) in višje energijsko območje (meritve v SPS-u). V tem vrstnem redu sta vrednosti šumnega člena enaki $(9.6 \pm 0.2)\%$ in $(25.5 \pm 2.2)\%$.

Tabela 1: Odvisnost energijske ločljivosti, pridobljene iz simulacij, od kota naklona prototipa in primerjava meritev s simulacijami pri naklonskem kotu $3^\circ + 3^\circ$.

naklonski kot	tip podatkov	vzorčevalni člen [%]	konstantni člen [%]
$2^\circ + 2^\circ$	simulacije	9.62 ± 0.05	1.33 ± 0.02
$3^\circ + 3^\circ$	simulacije	9.35 ± 0.05	1.08 ± 0.02
$3^\circ + 3^\circ$	meritve	9.75 ± 0.05	1.26 ± 0.01
$5^\circ + 3^\circ$	simulacije	9.20 ± 0.05	0.94 ± 0.02



Slika 3: Primerjava meritev s simulacijami pri naklonskem kotu $3^\circ + 3^\circ$.

Zaključek

Prototipni modul novega SpaCal kalorimetra z volframovim absorberjem in plastičnimi scintilacijskimi vlakni je bil testiran na pospeševalniku inštituta DESY v Hamburgu in pospeševalniku SPS Evropskega laboratorija za fiziko delcev - CERN. Prototip smo postavili v žarek pospešenih elektronov energij od 1 do 100 GeV in mu izmerili njegovo energijsko ločljivost in časovno ločljivost. Energijska ločljivost je znašala $\sim 9.75\%/\sqrt{E} \oplus 1.26\%$ pri naklonu prototipa za $3^\circ + 3^\circ$. Časovna ločljivost je znašala ~ 20 ps pri energiji žarka 100 GeV. Eksperimentalne meritve sem dodatno preveril s simulacijami in pokazal, da se rezultati relativno dobro ujema.